

2018

Radiosity Integral Equation Model for an Interior Space Illumination Design: Mars Project

Hien Ngo

Roger Williams University, hngo911@g.rwu.edu

Follow this and additional works at: https://docs.rwu.edu/math_theses

 Part of the [Mathematics Commons](#)

Recommended Citation

Ngo, Hien, "Radiosity Integral Equation Model for an Interior Space Illumination Design: Mars Project" (2018). *Mathematics Theses*.
5.
https://docs.rwu.edu/math_theses/5

This Thesis is brought to you for free and open access by the Feinstein College of Arts and Sciences Theses at DOCS@RWU. It has been accepted for inclusion in Mathematics Theses by an authorized administrator of DOCS@RWU. For more information, please contact mwu@rwu.edu.

Radiosity Integral Equation Model for an
Interior Space Illumination Design; Mars Project

Hien Ngo

Advisor: Dr. Yajni Warnapala

Bachelor of Science

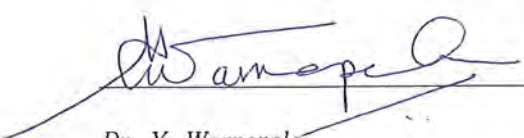
Mathematics Department

Feinstein College of Arts and Sciences

Roger Williams University

May 2018

The thesis of (Hien Ngo) was reviewed and approved by the following:

 _____ Date 4/19/2018

Dr. Y. Warnapala

Chair, Professor of Mathematics

Thesis Advisor

 _____ Date 4/19/2018

Dr. E. Dougherty

Professor of Mathematics

 _____ Date 4/20/2018

Dr. L. Guralnick

Professor of Biology

Acknowledgements

Thank you to Dr. Lonnie Guralnick and Dr. Edward Dougherty for being on the thesis committee for this research. Thank you Jim Lemire, Patricia Kennedy, Cheryl Francis, Professor Earl Gladue for their continuous support. Thank you to Dr. Yajni Warnapala. Without you, this thesis would not have been possible. This research was funded by the Rhode Island NASA Space Grant, the Mark Gould Research Scholarship and Research Award, the Roger Williams University Summer Undergraduate Research (SURF) Housing Program, the Roger Williams University Provost's Fund, and the Student Travel Grants from the Joint Mathematics Meeting.

Contents

| | |
|---|-----------|
| Acknowledgements | 2 |
| Abstract | 6 |
| 1 Introduction | 1 |
| 2 Methods | 3 |
| 2.1 Radiosity Integral Equation Model | 3 |
| 2.2 Dirichlet Condition | 4 |
| 2.3 Integral Equations | 4 |
| 2.4 Kernel | 6 |
| 2.5 Finite Element Method | 7 |
| 2.6 Galerkin Method of Weighted Residuals | 7 |
| 2.7 Gaussian Quadrature | 8 |
| 2.8 Green's Theorem | 9 |
| 2.9 Spherical Quatrefoil | 9 |
| 2.10 Emissivity and Reflectivity | 10 |
| 2.11 Fortran 77 | 12 |
| 2.12 Emissivity Functions | 13 |
| 2.13 Case 1: Brightness from External Light Source | 13 |
| 2.14 Limitations | 14 |
| 2.15 Case 2: Brightness from an Internal Light Source | 15 |
| 3 Results | 16 |
| 3.1 Spherical Quatrefoil and Simulation Parameters | 16 |
| 3.2 Numerical Results for Case 1 | 18 |
| 3.3 Numerical Results for Case 2 | 22 |
| 4 Discussion | 28 |
| 4.1 Thermal Control | 29 |
| 4.2 Design of Spherical Quatrefoil | 30 |
| 4.3 Rendering of Visual Model | 33 |
| 4.4 Future Direction | 35 |
| References | 37 |
| Appendices | 38 |
| A Surface Area | 38 |
| B Volume | 39 |
| C Maxwell Equations | 40 |
| D Volterra Integral Equations | 40 |
| E The Modified Decomposition Method | 42 |
| F The Adomian Decomposition Method | 43 |
| G The Direct Computation Method | 44 |
| H Finite Difference Method | 45 |
| I Legendre Polynomials | 46 |

| | | |
|----------|------------------------------------|-----------|
| J | Runge-Kutta Methods | 50 |
| K | Gaussian Quadrature Example | 51 |

List of Figures

| | | |
|----|---|----|
| 1 | Maple software rendering of the smooth, continuous, simply-connected, and bounded Spherical Quatrefoil. | 10 |
| 2 | Ambient or incident and reflecting beams interacting on a smooth surface with uniform reflectivity. | 10 |
| 3 | Programmed subroutine syntax using parametric equations (<i>Equation 2.11</i>) in Fortran 77 to generate absolute convergence error for the Spherical Quatrefoil. | 12 |
| 4 | The Martian sky at non imaged by Mars Pathfinder in June of 1999. This image was taken near local noon on Sol 10. A calibrated output device was required to accurately reproduce the correct color image [16]. | 13 |
| 5 | Plotted sinusoidal and cosinusoidal periodic functions as the true emissivity function in Case 1. | 14 |
| 6 | Convergence results for different points for the true function of $U_1 = 3\cos(2.18 \times 10^{-15}X + 3.92 \times 10^{-6}Y)$. A wave number 2.18×10^{-15} , an angular frequency 3.92×10^{-6} , $\rho = 0.10$, $NDEG = 5$, $NINTI = 32$, $NINTE = 8$, and a coefficient ratio of 1 : 2 : 1 for the Spherical Quatrefoil was used. | 20 |
| 7 | Convergence results for different points for the true function of $U_2 = 3.05\cos(2.18 \times 10^{-15}X + 3.92 \times 10^{-6}Y)$. A wave number 2.18×10^{-15} , an angular frequency was 3.92×10^{-6} , $\rho = 0.10$, $NDEG = 5$, $NINTI = 32$, $NINTE = 8$, and a coefficient ratio of 1 : 2 : 1 for the Spherical Quatrefoil was used. | 20 |
| 8 | Convergence results for different points for the true function of $U_3 = 0.0003\sin(2.18 \times 10^{-15}X + 3.92 \times 10^{-6}Y)$. A wave number 2.18×10^{-15} , an angular frequency was 3.92×10^{-6} , $\rho = 0.10$, $NDEG = 5$, $NINTI = 32$, $NINTE = 8$, and a coefficient ratio of 1 : 2 : 1 for the Spherical Quatrefoil was used. | 21 |
| 9 | Convergence results for different points for the true function of $U_4 = 0.00003\sin(2.18 \times 10^{-15}X + 3.92 \times 10^{-6}Y)$. The wave number was 2.18×10^{-15} , the angular frequency was 3.92×10^{-6} , $\rho = 0.10$, $NDEG = 5$, $NINTI = 32$, $NINTE = 8$, and a coefficient ratio of 1 : 2 : 1 for the Spherical Quatrefoil was used. | 21 |
| 10 | Convergence results for blue emissivity sine function. Emissivity given by $U = \sin(1.58 \times 10^{-15}X - 4.72 \times 10^{-21}Y)$. A coefficient ratio of 1 : 2 : 1 for the Spherical Quatrefoil and $\rho = 0.004$ was used. $NDEG = 5$, $NINTI = 32$, and $NINTE = 8$. Four different directions of the same distance were used. | 23 |
| 11 | Convergence results for blue emissivity sine function. Emissivity given by $U = \cos(1.58 \times 10^{-15}X - 4.72 \times 10^{-21}Y)$. A coefficient ratio of 1 : 2 : 1 for the Spherical Quatrefoil and $\rho = 0.004$ was used. $NDEG = 5$, $NINTI = 32$, and $NINTE = 8$. Four different directions of the same distance were used. | 23 |
| 12 | Optimal convergence results for blue light emissivity function of a sine function for various points using an amplitude of 10; emissivity given by $U_5 = 10\sin(1.58 \times 10^{-15}X - 4.72 \times 10^{-21}Y)$, $\rho = 0.004$, and a coefficient ratio of 1 : 2 : 1 for the Spherical Quatrefoil was used. $NDEG = 5$, $NINTI = 32$, and $NINTE = 8$. Four different points with increasing distance from the boundary of the shape were used. Values of absolute error have been truncated for scaling of identifying differences. | 24 |
| 13 | Convergence results for blue emissivity sine function. Emissivity given by $U = 10\sin(1.58 \times 10^{-15}X - 4.72 \times 10^{-21}Y)$, and a coefficient ratio of 1 : 2 : 1 for the Spherical Quatrefoil and a distance of 11.8034 was used. $NDEG = 5$, $NINTI = 32$, and $NINTE = 8$. Various diffuse reflectance values were used in the calculation of reflectivity. | 25 |

| | | |
|----|---|----|
| 14 | Convergence results for blue emissivity sine function. Emissivity given by $U = 10\sin(1.58 \times 10^{-15}X - 4.72 \times 10^{-21}Y)$, $\rho = 0.013625$, and a coefficient ratio of 0.95 : 2.07 : 1 for the Spherical Quatrefoil was used. $NDEG = 5$, $NINTI = 32$, and $NINTE = 8$. This simulation utilizes optimal amplitude, diffuse reflectivity, various points with increasing distance with the source positioned from the top relative to the exterior boundary. | 27 |
| 15 | A preliminary sketch of the Spherical Quatrefoil and its interior configuration with its original ratio of 1:1:1. | 29 |
| 16 | Updated layout of interior space capsule consisting of basic workstation panels and controlling system consoles on both ends surrounding four seats mapped and drawn out. | 30 |
| 17 | Perspective of interior arrangement from a stored point of view with mocked Martian sky and blue light flooring. | 31 |
| 18 | Phases I-IV of MAV Case 1 and Case 2 installations over the course of 65 hours. | 34 |
| 19 | Interior of MAV simulates design for numerical results of Case 2 Brightness from an internal artificial light source. | 34 |
| 20 | Snapshot of triple integral to approximate volume in Python. | 39 |
| 21 | Screen capture of system solved using Wolfram Mathematica 11. | 47 |
| 22 | Solving for roots of the Legendre polynomial of degree 5. | 48 |
| 23 | 26 sets of high accuracy Gaussian Quadrature nodes and weights from the Keisan Online Calculator service provided by Casio ComputerCo., Ltd. | 49 |

List of Tables

| | | |
|---|--|----|
| 1 | Weighted emissivity and reflectivity values in accordance with proportions of interior space. . | 11 |
| 2 | Convergence errors were calculated for different directions and increasing distances, a reflectivity value of $\rho = 0.004$, $NINTE = 32$, and $NINTE = 20$. Various degrees of the boundary function were tested to find optimal convergence. | 16 |
| 3 | Convergence errors were calculated for different directions and increasing distances, a reflectivity value of $\rho = 0.004$, and boundary function degree $n = 5$. Various combinations of interior nodes and exterior nodes were tested for optimal convergence error. | 17 |
| 4 | Convergence errors were calculated for different directions and constant distance, a reflectivity value of $\rho = 0.004$, a boundary function degree $NDEG = 5$, $NINTE = 8$, and $NINTI = 32$. Various Spherical Quatrefoil ratios were tested for optimal convergence error . | 17 |
| 5 | Optimal amplitudes of different points for the true functions with wavelengths ranging from 625 nm to 659 nm of visible light. 2.18×10^{-15} as the wave number and 3.92×10^{-6} as the angular frequency, $\rho = 0.10$, $NDEG = 5$, $NINTI = 32$, $NINTE = 8$, and the coefficient ratio of 1:2:1 for the Spherical Quatrefoil. | 19 |
| 6 | Convergence results for blue emissivity sine function. Emissivity was given by $U = A\sin(1.58 \times 10^{-15}X - 4.72 \times 10^{-21}Y)$. A coefficient ratio of 1:2:1 for the Spherical Quatrefoil and $\rho = 0.004$ was used. $NDEG=5$, $NINTI=32$, and $NINTE=8$. From 4 different directions, 4 different amplitudes (1,2,5 and 10) were tested and 1 and 10 showed to be the most viable. . | 22 |
| 7 | Convergence results for blue emissivity sine function. Emissivity was given by $U_5 = 10\sin(1.58 \times 10^{-15}X - 4.72 \times 10^{-21}Y)$. A coefficient ratio of 1:2:1 for the Spherical Quatrefoil, $NDEG = 5$, $NINTI = 32$, and $NINTE = 8$ were used. Various diffuse reflectivity values were tested. Points are listed and their distances are 11.18034, 12.569805, 44.877611, and 134.632834 respectively. | 25 |
| 8 | Convergence results for blue emissivity sine function. Emissivity given by $U = 10\sin(1.58 \times 10^{-15}X - 4.72 \times 10^{-21}Y)$. A coefficient ratio of 1 : 2 : 1 for the Spherical Quatrefoil and a $\rho = 0.013625$ was used. $NDEG=5$, $NINTI=32$, and $NINTE=20$. Various points with increasing distance were used to evaluate optimal location of light source relative to the exterior boundary. | 26 |
| 9 | Convergence results for various degrees with $NINTI=32$, $NINTE=8$, and a $\rho = 0.013625$. Arbitrary points were used to show the effect of increasing $NDEG$ to 7, 11, and 13. | 36 |

Abstract

This research project is focused on finding the true solution of the exterior Dirichlet problem to determine the convergence results for the Spherical Quatrefoil using the Galerkin Method. A mathematical model, based on the Radiosity integral equation will be utilized to investigate the role of incoming light waves for different surfaces with various emissivity and reflectivity functions. Theoretical and computational details of the method will provide sufficient information for designing proper lighting of an interior space inside a habitat that can ultimately be used for future endeavors in Mars exploration.

1 Introduction

The National Aeronautics Space Administration (NASA) Authorization Act of 2017 was a recent development that emphasized getting humanity to Mars by the 2030s. A manned mission to Mars could teach us about Earth's history and life in the universe as well as the potential to jump start massive developments in areas such as recycling, solar energy, food production, and the advancement of medical technology. The pace of human missions to Mars is accelerating and it is crucial to plan for the journey of those astronauts. This research aims to apply the Radiosity integral equation and the Galerkin method to design illumination on the interior of a manned spacecraft to Mars. Numerical solutions with this Radiosity Integral equation model has also been done in a study of design parameters for space base and space shuttle heat rejection systems [3]. In addition, this method has been used to solve the exterior Dirichlet problem for the sphere, perturbation of the sphere, ellipsoid, the oval of Cassini in three dimensions, and the Spherical Rhombus [24]. This research will obtain numerical solutions for different emissivity and reflectivity functions to simulate brightness inside a newly generated Spherical Quatrefoil space with external and internal lighting mechanisms.

Proper lighting is one of the most important aspects in construction, architecture, and design work as it can highly impact human mental states, psychological needs, and physical health [5]. Light exposure can have numerous effects on the human circadian process through the non-imaging forming system [6]. As human explorers would be required to inhabit the same space for an extended period of time, designing brightness and illumination inside that space is essential for both ambiance and functionality. This can be done by extrapolating with the Radiosity integral equation model, current data for space exploration, and conditions on planet Mars.

It is known that Mars is a terrestrial planet composed of a thin atmosphere; primarily of 95% carbon dioxide. There are routine oxidized iron dust storms, snow fall in the form of fog composed of carbon dioxide, and seasonal changes similar to those experienced on Earth. Unlike the Earth, it does not contain a global magnetic field to protect from radiation [12]. Due to this difference, there is a higher fraction of solar energy that reaches the surface of the planet. Currently, scientists continue searching and testing the surface and atmospheric radiation in the Martian environment. One aspect of this endeavor is to under-

stand how these conditions could affect communication and navigation systems on a spacecraft. Emissivity on Mars requires further research, but it has been found that Martian surface emissivity is closely related to its physical temperature. Even more, it was discovered that planet Mars generally has larger surface emissivity and higher brightness temperatures compared to that of Earth's [10].

Electromagnetic radiation can be absorbed, transmitted, and scattered by particles in the atmosphere. Scattering is the redirection of electromagnetic energy by suspended particles. The type and the amount of scattering that occurs depends on size of the particles and wavelength of the energy. The main types of scattering that impact incoming solar radiation are Rayleigh scatter, Mie scatter, and non-selective scatter. Humans are most familiar with Rayleigh scattering on Earth's thick atmosphere. Rayleigh scattering occurs when radiation (light) interacts with molecules and particles in the atmosphere that are smaller than the wavelength of the incoming radiation. On Earth, a blue sky appears during the day and an orange sun sets in the evening due to the scattering of sunlight by microscopic particles. The atmosphere on Mars contains a significant amount of fine particulate. As a result, the scattering effect is nearly the opposite; blue light penetrates the atmosphere more efficiently, scatters off the dust, and stays closest to the direction of the sun. Therefore, a blue tinted sunset can be observed on Mars.

It is known that wavelengths of blue light are relatively shorter and contain higher amounts of energy compared to others in the visible spectrum. This allows for them to scatter more efficiently by molecules in the atmosphere. Humans experience the sight of a blue sky daily and the human body has learned to use blue light from the sun to regulate natural sleep and wake cycles, also known as circadian rhythm. Blue light has also been found to help humans stay alert by heightening their reaction times, elevating their moods, and increasing the feeling of overall well being [11]. In our research, we extrapolate with information of scattering on Earth and emissivity on Mars to direct our simulations using the Radiosity integral equation model. If there is potential to harness radiation from the Sun, it can be simulated to generate numerical results; we name this Case 1. In addition to this scenario, we investigate alternative means of illumination; for instance, an artificial light source within the habitat (Case 2) as fluorescent lamps have also been reported to be the most appropriate light source for the illumination on the interior of a spacecraft [25].

2 Methods

2.1 Radiosity Integral Equation Model

The Radiosity Integral equation is the foundation of this research. It is a mathematical model for the brightness of a collection of one or more surfaces when their reflectivity and emissivity components are given. The model has been used in studying computer graphics as it provides solutions for more realistic illumination on the display of surfaces [1]. It simultaneously allows a numerical solution for brightness and a physical model of indirect diffuse illumination. If S is a closed and bounded surface, P is a point of light, or $P \in S$, then it can be given by,

$$u(P) - \frac{\rho(P)}{\pi} \int_s u(Q)G(P, Q)V(P, Q)dS_Q = E(P) \quad (2.1)$$

Radiosity or the brightness is represented by $U(P)$, emissivity is represented by $E(P)$, reflectivity represented as $\rho(P)$ with both reflectivity and emissivity values between 0 and 1. The Radiosity model transforms the light transfers into a system of linear equations. In this research we solve for the Dirichlet condition which assumes that all incoming light waves are absorbed by the outer surface, thus $U(P) = E(P)$. The kernel $G(P, Q)$ is given by,

$$G(P, Q) = \frac{[(Q - P) \cdot n_P][(P - Q) \cdot n_P]}{|P - Q|^4} \quad (2.2)$$

and it is assumed here that the points P and Q do not intersect the surface at any other point, and so n_P is an inner unit normal to S at P , and $V(P, Q)=1$ on an unclouded surface. The kernel has the characteristic of being weakly singular, which eliminates and avoids an issue of implosion where there is no fog or transmission. The exterior boundary problem for the Spherical Quatrefoil is solved using the Gaussian Quadrature Method, in which rotations of the coordinates minimize the inherent singularity that is present in the fundamental solution. The Dirichlet boundary condition takes into account the absorption of the incoming light waves and assumes that the surfaces are Lambertian diffuse reflectors. Nevertheless, brightness of these surfaces are the same regardless of the observer's angle of view. We will assume that

the true solution of the Radiosity integral equation model is equal to emissivity ($U(P) = E(P)$) and utilize Galerkin coefficients to calculate the convergence errors between the true solutions and the approximated solutions in Fortran 77.

2.2 Dirichlet Condition

Boundary conditions are often set on solutions when solving for differential equations. The Dirichlet condition is sufficient for a real-valued, periodic function. Let f be a bounded function that is absolutely integrable with a finite number of maxima and minima within the bounded interval. In addition, f also must have a finite number of discontinuities. The condition is given by,

$$\sum_{n=-\infty}^{\infty} \frac{1}{2}(f(x_n+) + f(x_n-))$$

Here, the Fourier series for f converges and is equal to f wherever f is continuous. This approach analyzes the integral on the boundary and transforms the region to a line integral.

2.3 Integral Equations

There are four basic types of integral equations each involving an unknown function $\rho(y)$ in an integral with a kernel $K(x, y)$ and all have an input function $f(x)$. Volterra Equation of the first kind,

$$\int_a^b K(x, y)\rho(y)dy = f(x)$$

Volterra equation of the second kind,

$$\rho(x) - \int_a^b K(x, y)\rho(y)dy = f(x)$$

Fredholm equation of the first kind,

$$\int_a^b K(x, y)\rho(y)dy = f(x)$$

and Fredholm equation of the second kind

$$\rho(x) - \int_a^b K(x, y)\rho(y)dy = f(x).$$

Equations of the first kind involve the unknown function $\rho(y)$ inside the integral. The Radiosity integral equation that we use in this research involves $\rho(y)$ outside the integral and can be described as a nonlinear weakly-singular Fredholm integral equation. These types of equations often arise in practical

applications such as computing conformal mappings and determining the propagation of waves. The equation has the general form shown by,

$$u(t) = f(t) + \lambda \int_a^b K(t, s)\phi(s)ds \quad (2.3)$$

Since our Fredholm integral equation of the second kind is nonlinear and singular, commonly used methods such as the Modified Decomposition Method, the Adomian Decomposition Method, and the Direct Computation method fail (See Appendix E, F, and G). The Radiosity integral equation has been studied for occluded surfaces using a Collocation method. Numerical results on the planar Radiosity integral equation have been obtained using a matrix-vector multiplication method [1]. In our research, the solutions for the Radiosity integral equation will be solved using the Galerkin method with weighted residuals.

2.4 Kernel

In order to solve for brightness $u(P)$ would integrate $u(Q)$ within a closed bounded surface at an exterior point with respect to Q . We have $G(P, Q)$ as the kernel in the Radiosity equation. It is given by,

$$G(P, Q) = \frac{\cos(\theta_P) \cdot \cos(\theta_Q)}{|P - Q|^2} = \frac{[(Q - P) \cdot n_P][(P - Q) \cdot n_Q]}{|P - Q|^2}$$

where n_P and n_Q are the inner unit normals to S at P and Q . Here we show that the Kernel is weakly-singular by letting $P = (p_1, p_2, p_3)$, and $Q = q_1, q_2, q_3$

$$\begin{aligned} n_P &= \frac{(p_1, p_2, p_3)}{\sqrt{p_1^2 + p_2^2 + p_3^2}}, n_Q = \frac{(q_1, q_2, q_3)}{\sqrt{q_1^2 + q_2^2 + q_3^2}} \\ (Q - P) &= (q_1 - p_1, q_2 - p_2, q_3 - p_3) \\ (P - Q) &= (p_1 - q_1, p_2 - q_2, p_3 - q_3) \end{aligned}$$

we can write,

$$[(Q - P) \cdot n_P][(P - Q) \cdot n_Q] = [(Q - P) \cdot (P - Q)][n_P \cdot n_Q]$$

thus,

$$[(q_1 - p_1, q_2 - p_2, q_3 - p_3) \cdot (p_1 - q_1, p_2 - q_2, p_3 - q_3)][n_P \cdot n_Q]$$

$$[(Q - P) \cdot n_P][(P - Q) \cdot n_Q] = -[(p_1 - q_1)^2 + (p_2 - q_2)^2 + (p_3 - q_3)^2][n_P \cdot n_Q]$$

where $n_P \cdot n_Q$ is the dot product and so it would give a constant.

$$\begin{aligned} n_P \cdot n_Q &= \frac{(p_1, p_2, p_3)}{\sqrt{p_1^2 + p_2^2 + p_3^2}} \cdot \frac{(q_1, q_2, q_3)}{\sqrt{q_1^2 + q_2^2 + q_3^2}} = \frac{(p_1 q_1 + p_2 q_2 + p_3 q_3)}{\sqrt{(p_1^2 + p_2^2 + p_3^2)(q_1^2 + q_2^2 + q_3^2)}} \\ |P - Q| &= \sqrt{(p_1 - q_1)^2 + (p_2 - q_2)^2 + (p_3 - q_3)^2} \\ |P - Q|^4 &= [\sqrt{(p_1 - q_1)^2 + (p_2 - q_2)^2 + (p_3 - q_3)^2}]^2 \\ \frac{[(Q - P) \cdot n_P][(P - Q) \cdot n_Q]}{|P - Q|^4} &= \frac{-[(p_1 - q_1)^2 + (p_2 - q_2)^2 + (p_3 - q_3)^2][n_P \cdot n_Q]}{[(p_1 - q_1)^2 + (p_2 - q_2)^2 + (p_3 - q_3)^2]^2} \\ &= \frac{[(Q - P) \cdot n_P][(P - Q) \cdot n_Q]}{(p_1 - q_1)^2 + (p_2 - q_2)^2 + (p_3 - q_3)^2} \end{aligned}$$

From the kernel, $u(Q)$ is eliminated in the integration process and so the Kernel is proved to be weakly-singular. This prevents the direct integration to find brightness, $u(P)$, from the Radiosity integral equation. It is thus necessary that the solution to this equation be numerically approximated.

2.5 Finite Element Method

Our research method encompasses important theories and formulations of a numerical approximation methods. This integral equation approach is widely recognized as an efficient approach for solving exterior boundary value problems such as the Radiosity equation. The Finite Element Method (FEM) divides a three-dimensional structure into several elements, reconnects them with nodes to result in a set of a system of algebraic equations. Each element is composed of interior and exterior nodes where the latter are defined by the boundary conditions. In connecting the individual elements, the entire field quantity becomes interpolated over the entire structure in a piecewise manner [7]. Moreover, this method can minimize integrals and bound them by differentiable functions that satisfy certain boundary conditions. The Galerkin method using weighted residuals that is used in this research is derived from the FEM.

2.6 Galerkin Method of Weighted Residuals

Weighted Residual methods (WRM) analytically approximate solutions in a piecewise manner. Generally, the solution of a partial differential equation can be expressed using a base set of functions (basis) where the coefficients can be determined using a chosen method. The Galerkin method of Weighted Residuals is a subclass of Weighted Residual methods which can be used to solve differential equations and to derive the element equations for the FEM. This method will allow for different nodes and various distances in evaluating over spherical surfaces [14]. Nonetheless, it can be used to approximate the solutions for spherical shapes such as the one featured in this research. The solution in Galerkin's method is given by,

$$u_{\hat{N}} = \sum_{j=1}^d \alpha_j \quad (2.4)$$

$$\alpha_i(h_i, h_i) - \sum_{j=1}^d \alpha_j (\hat{G}h_j, h_i) = (\hat{E}, h_i) \quad (2.5)$$

where $u_{\hat{N}}$ is Radiosity, G is the kernel term, and E is emissivity. The coefficients $(\hat{G}h_j, h_i)$ are fourfold integrals with a singular integrand. To calculate $\hat{G}h_j$, the surface S is rotated such that P is not a singular point internal to the integration region. Therefore, the Galerkin coefficients only rely on the surface S . In this method, weight functions are chosen to be identical to the base functions. For simulations in For-

tran 77, let NINTI denote the interior nodes needed for calculating $\hat{G}h_j$, NINTE denote the exterior nodes needed for calculating $(\hat{G}h_j, h_i)$, and NDEG denote the approximating degree of spherical harmonics.

2.7 Gaussian Quadrature

In order to apply the aforementioned method, it is necessary to define the boundary and the basis function. Using a numerical quadrature by interpolating associated polynomials is a basic method in approximating an integral when there is no explicit anti-derivative for the function (See Appendix L). The numerical approximation of the definite integral is usually stated as a weighted sum of function values at specified points within the domain of integration. The nodes or roots $X_1, X_2, X_3 \dots X_n$ in $[a, b]$ and coefficients $C_1, C_2, C_3 \dots C_n$, are chosen to minimize expected error obtained in the approximation.

$$\int_a^b f(x)dx \approx \sum_{i=1}^n C_i f(X_i) \quad (2.6)$$

If $X_1 \dots X_n$ are the roots of the n^{th} Legendre polynomial $P_n(x)$, then

$$C_i = \int_{-1}^1 \prod_{j=1}^n \left(\frac{X - X_j}{X_i - X_j} \right) dx \quad (2.7)$$

Since the method is defined in $[-1, 1]$, the integral's interval $[a, b]$ or $\int_a^b f(x)dx$ must be converted using a change of variables equation:

$$t = \frac{2x - a - b}{b - a} \quad (2.8)$$

The method can then be applied on $[a, b]$.

$$\int_a^b f(x)dx = \int_{-1}^1 f\left(\frac{(b-a)t + (b+a)}{2}\right) \left(\frac{b-a}{2}\right) dt \quad (2.9)$$

Since the region consists of unequal step sizes, it is advantageous that this method chooses the points for evaluation in an optimal rather than an equally spaced way. For our research, we have chosen the spherical harmonic function as the basis function. More specifically, Legendre Polynomials and its associated functions define our subspaces (See Appendix I).

2.8 Green's Theorem

In order to find the true solution of the exterior Dirichlet problem for the Radiosity equation, the general equations governing a sphere can be used to derive a form that is closed, bounded, and simply-connected. These are the conditions prescribed by Green's Theorem. Fulfilling these conditions allows for the analysis of the integral over a boundary. Given a smooth and simply connected region S , the double integral over S can be transformed into a line integral given by,

$$\int \int_S \left(\frac{\partial Q}{\partial x} - \frac{\partial P}{\partial y} \right) dA = \oint_{\partial S} (P dx + Q dy) \quad (2.10)$$

In order to solve the Radiosity integral equation, it is necessary to abide by Green's Theorem as to allow differentiability along a shape's boundaries.

2.9 Spherical Quatrefoil

The Spherical Quatrefoil form was generated using Maple software and the general equations governing a sphere [17]. In two dimensions, the Quatrefoil is a carved ornament having four foils or leaflets arranged around a common center. It is a well-adapted motif seen in architecture work of the Gothic and Renaissance eras. In three dimensions, the Spherical Quatrefoil can be defined in a spherical coordinate system with a radius defined as,

$$\rho = 0.002 + 0.003 \cos(2\theta)^2$$

and three parametric equations given by,

$$\begin{aligned} x &= (0.95)\rho \sin \theta \cos \phi \\ y &= (2.07)\rho \sin \theta \sin \phi \\ z &= (0.99)\rho \cos \theta \end{aligned} \quad (2.11)$$

for the boundaries,

$$0 < \theta < \pi \quad 0 < \phi < 2\pi \quad 0 \leq \cos 2\theta \leq 1$$

where θ is the polar angle from the positive z-axis and ϕ is the angle from the x-axis in the xy-plane.

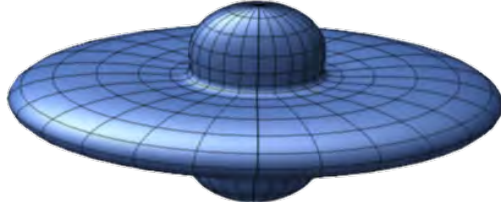


Figure 1: Maple software rendering of the smooth, continuous, simply-connected, and bounded Spherical Quatrefoil.

The Spherical Quatrefoil is a bilaterally symmetrical shape having a long horizontal elliptical body with vertical nodes protruding from above and below its base. The surface area of the smooth and spherical shape is irregular, but can be approximated using oblate and prolate spheroid surface area formulas. The quantity of the space enclosed by the shape can be solved by deriving a volume integral using its parametric equations (See Appendix B).

2.10 Emissivity and Reflectivity

Reflectivity is the physical property that measures a material surface's ability to reflect light rays. It is characterized as a ratio with values ranging between 0 and 1 to define the amount of reflected solar radiation flux to the incident flux. Reflection that occurs off of smooth surfaces are called specular reflection while that of which occurs off of rough surfaces are known as diffuse reflection (Figure 2). Reflectivity depends on the energy of the wavelength, the geometry of the surface, and the surface material. Differences in reflectivity have been identified for many different materials by analysis of spectral reflectance curves as a function of wavelengths. These reflectivity values will be used in creating our model for simulation. In reality, most of the surfaces on earth are neither perfectly specular or diffuse reflectors, but their characteristics are a combination of the two types. For our purposes of parametrization, we will idealize that all surfaces are diffuse or Lambertian reflectors and that they reflect uniformly in all directions.

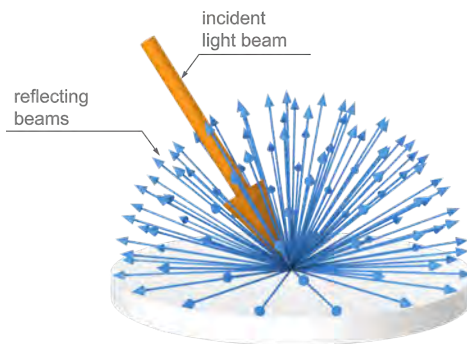


Figure 2: Ambient or incident and reflecting beams interacting on a smooth surface with uniform reflectivity.

Emissivity is a surface property that measures a material surface’s thermal emittance or the ability to release absorbed heat. It has also been defined as a value between 0 and 1 in order to express the radiation of absorbed energy.

$$1 = E(P) + \rho(P)$$

In the equation shown above, both properties exhibit an inversely proportional relationship due to the fact that most objects exhibit low transmission of infrared energy. There have been published emissivity and reflectivity values for metal alloys and manufactured carbon-based fibers which could be used as inputs for the Radiosity integral equation model [8]. The emissivity of materials appropriate for space travel were identified. Simulations then account interactions of materials and light waves inside the structure. To investigate brightness, various boundary functions and weighted averages for reflectivity were used to generate convergence data (Table 1).

Table 1: Weighted emissivity and reflectivity values in accordance with proportions of interior space.

| Material | Emissivity | Reflectivity |
|--|------------|--------------|
| Space Gray SPIREX SP102 | 0.490 | 0.02 |
| Quartz/Rough/Fused | 0.167 | 0.015 |
| Black Velvet Coating 9560 Series Optical | 0.168 | 0.01 |
| Zinc Oxide/White Coating | 0.095 | 0.05 |
| Weighted Average | 0.490 | 0.02 |

2.11 Fortran 77

Various formulas and values will be used as either functions or inputs into the Fortran 77 program to simulate scenarios in which the Spherical Quatrefoil is inhabited by human explorers while docked on planet Mars. Parameters will be assumed based on published research and laboratory tested reports of commercial spacecrafts. Constraints and different boundary conditions will be tested and investigated to generate convergence results with the most accuracy and the smallest absolute error. It should be noted that Fortran 77 absolute error is generated with double precision.

```
C      THIS IS A SPHERICAL QUATREFOIL REGION
60     CST2T=CST*CST-SNT*SNT
      SN2T=TWO*SNT*CST
      R=0.002+0.003*(CS2T)**2
      X=A*R+SNT*CSP
      Y=B*R+SNT*SNP
      Z=C*R**CST
      DX(1)=-R*A+SNT*SNP
      DX(2)=A*CSP*R+CST-12*CS2T*SN2T*SNT
      DY(1)=B*R*SNT*CSP
      DY(2)=B*SNP*(R*CST-12*(CS2T*SN2T*SNT))
      DZ(1)=C*ZERO
      DZ(2)=-12*C*CS2T*SN2T*CST-R*SNT
      RETURN
      END
```

Figure 3: Programmed subroutine syntax using parametric equations (*Equation 2.11*) in Fortran 77 to generate absolute convergence error for the Spherical Quatrefoil.

The data generated will depend mainly on the constraints set on the different inputs for emissivity, values for reflectivity, the number of interior (NINTI) integration nodes, the number of exterior (NINTE) integration nodes, the various oscillation functions for emissivity, and the degree of boundary functions used.

2.12 Emissivity Functions

It is known that surface reflectivity and emissivity have a radio frequency dependence. The concepts of Rayleigh scattering and periodic functions to model light interactions allow for emissivity functions as inputs of the Radiosity integral equation model. For testing this scenario, a second-order linear partial differential wave equation was used to model the interaction between light components such as wavelength (λ), frequency (ν), angular frequency (ω), wave number (k), time in seconds (t), and amplitude (A).

$$y = A \sin(kx - \omega t) \tag{2.12}$$

2.13 Case 1: Brightness from External Light Source

The first scenario we call Case 1 describes the potential to harness external lighting from the Sun for illumination at the time that humans are stationed on planet Mars. The precise color of the Martian sky has been measured and analyzed at the pathfinder landing sites and researchers have been able to measure scattered light from the sky. With visual imaging from the intel of rovers, the Martian sky has been described to be a butterscotch color at midday on the planet. For the naked human eye, the sunlight that shines onto Mars renders a warm red-orange appearance partly due to the presence of the iron(III) oxide dust [18].



Figure 4: The Martian sky at non imaged by Mars Pathfinder in June of 1999. This image was taken near local noon on Sol 10. A calibrated output device was required to accurately reproduce the correct color image [16].

When light radiates from the Sun and shines onto Mars, the sky appears to be orange in color. The wavelength and frequency values will be derived from orange visible light on the electromagnetic spectrum. In using the wavelength of orange visible light as the input of both the functions, it is necessary to obtain an optimal range of varying amplitude. Amplitude of a light wave is important in understanding the brightness or intensity of the light as it measures the amount of energy carried. Since there have not yet

been specific amplitude values reported from planet Mars, ranges will be obtained according to convergence results with the smallest absolute error for the sine function and its cofunction.

Convergence results for both oscillatory functions in low energy conditions were generated. For our purposes, numerical solutions were generated with large distance due to the way external lighting would be located far away relative to the spacecraft or habitat. The points used in these simulations have a scalable distance of 374.167 units and are illustrative of penetrating light beams.

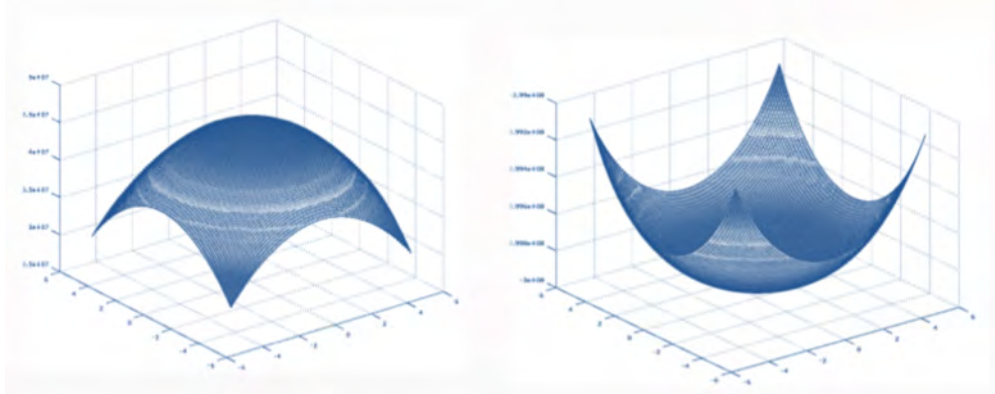


Figure 5: Plotted sinusoidal and cosinusoidal periodic functions as the true emissivity function in Case 1.

2.14 Limitations

There are inevitable limitations to using convergence results generated using the Radiosity Integral equation. For example, it has been known that there are storms that kick up oxidized iron dust that are capable of blanketing large areas of the planet Mars' surface. These occurrences were not accounted for in the selective absorption and scattering of light for the true emissivity functions in Case 1. In this case, Mars explorers' would not be able to rely on the Sun for an external light source and would consequently need at least an artificial light source in their spacecraft.

Another concern is that while the lack of a global magnetic field on Mars allows for a higher fraction of solar energy to reach the planet's surface and could be advantageous in providing illumination, it eliminates a source of protection from harmful radiation. Energetic particles can cause radiation sickness and the risk for cancer given by waves and sub-atomic particles. On Earth, the atmosphere naturally protects humans by blocking most of these particles from ever reaching the surface. NASA is currently conducting studies and research on various methods and materials such as electrical hardware to protect astronauts from space radiation. Significant development in these technologies would be required in order to apply

Case 1's mode of illumination. Meanwhile, we investigate alternative modes of illumination to optimize brightness.

2.15 Case 2: Brightness from an Internal Light Source

A second scenario we call Case 2 models the illumination inside the Spherical Quatrefoil with an internal artificial light source. In order to maintain the mathematical integrity of our model, the Spherical Quatrefoil can be made into the form of a room within a larger spacecraft. In this way, the conditions of our exterior boundary problem is still fulfilled and Radiosity can be accounted for. Since these simulations implement a light source at a closer distance in proximity to the interior space and the surfaces inside, it is necessary to have a more perceptive understanding of the the room's arrangement. More specifically, the positioning of the light and the type of light should be investigated. While the former can be designed using the numerical results that are found, the latter requires some intuition and literature mining.

Research data has made it evident that colors have the ability to affect human psychology, biology, and physiological [2]. Research has reported that short-wavelength blue light can be greatly efficient in maintaining synchronized circadian rhythms. The stresses of spaceflight can lead to poor sleep quality and result impair alertness, reaction time, and cognition. Studies have shown that light treatment have the ability to correct those impairments. There are researchers who aim to develop in-flight lighting to enhance alertness in astronauts as well as NASA's ground crew. Research on human behavioral health and performance by individuals at the Jefferson Medical College of Thomas Jefferson University are studying the efficacy of blue-enriched polychromatic solid-state light for acutely enhancing alertness and cognitive performance during spaceflight [4]. The effectiveness of blue light LED lights are being tested for possible use in the International Space Station as well as vehicles and habitats being developed for future space missions [4]. Case 2 models the illumination inside the spacecraft just outside the Spherical Quatrefoil with an internal artificial a short-wavelength blue light source. In maintaining the mathematical conditions to our exterior boundary problem, a practical concept for illumination implies smaller distances in our simulations. In addition, wavelength and frequency values on the visible light spectrum (blue light) can be integrated into our emissivity functions.

3 Results

3.1 Spherical Quatrefoil and Simulation Parameters

The absolute convergence error between true solutions and numerical approximations were generated in Fortran 77. When approximating solutions in numerical analysis, a convergence error less than or equal to 10^{-5} is sufficient and acceptable. These convergence results can be used to compare and optimize the shape of the Spherical Quatrefoil for varying degrees of boundary functions ($NDEG$), interior nodes ($NINTI$), exterior nodes ($NINTE$), and points (X, Y, Z). More specifically, $n = \langle 3, 5, 7 \rangle$; $NINTI = \langle 16, 32 \rangle$; $NINTE = \langle 8, 16, 20 \rangle$ in combination with exterior points which vary in distance and direction. For the purposes of these simulations the units of distance are constant and arbitrary. The following results illustrate this process. These convergence error results indicate that setting a degree of 5 produces smaller absolute error to two decimal places in comparison to that of degree 7 and 3. It is evident that both underestimating and overestimating the degree of boundary function affects our convergence error results.

Table 2: Convergence errors were calculated for different directions and increasing distances, a reflectivity value of $\rho = 0.004$, $NINTI = 32$, and $NINTE = 20$. Various degrees of the boundary function were tested to find optimal convergence.

| Degree | Distance | Points (X,Y,Z) | Absolute Error |
|--------|------------|----------------|------------------|
| 3 | 9.899495 | 3,5,8 | 3.0723900010D-04 |
| | 13.747727 | -5,8,10 | 3.0723899844D-04 |
| | 53.851648 | 20,-30,40 | 3.0723899998D-04 |
| | 728.010989 | 100,400,600 | 3.0723898504D-04 |
| 5 | 9.899495 | 3,5,8 | 9.3177835865D-06 |
| | 13.747727 | -5,8,10 | 9.3177822218D-06 |
| | 53.851648 | 20,-30,40 | 9.3177863608D-06 |
| | 728.010989 | 100,400,600 | 9.3177989215D-06 |
| 7 | 9.899495 | 3,5,8 | 1.3685226805D-04 |
| | 13.747727 | -5,8,10 | 1.3685226898D-04 |
| | 53.851648 | 20,-30,40 | 1.3685226565D-04 |
| | 728.010989 | 100,400,600 | 1.3685225275D-04 |

Table 3 displays simulations with absolute error tolerance for various interior and exterior node combinations. We note that 32 interior nodes and 8 exterior nodes produce the smallest absolute errors which we can use to generate convergence results for solving the Radiosity integral equation using the Galerkin Method.

Table 3: Convergence errors were calculated for different directions and increasing distances, a reflectivity value of $\rho = 0.004$, and boundary function degree $n = 5$. Various combinations of interior nodes and exterior nodes were tested for optimal convergence error.

| Exterior Nodes | Interior Nodes | Points (X,Y,Z) | Absolute Error |
|----------------|----------------|----------------|------------------|
| 8 | 16 | 3,5,8 | 2.3916801559D-05 |
| | | -5,8,10 | 2.3916799758D-05 |
| | | 20,-30,40 | 2.3916804622D-05 |
| | | 100,400,600 | 2.3916816881D-05 |
| 16 | 32 | 3,5,8 | 1.0482505537D-05 |
| | | -5,8,10 | 1.0482504145D-05 |
| | | 20,-30,40 | 1.0482508334D-05 |
| | | 100,400,600 | 1.0482508334D-05 |
| 8 | 32 | 3,5,8 | 9.3177835865D-06 |
| | | -5,8,10 | 9.3177822218D-06 |
| | | 20,-30,40 | 9.3177863608D-06 |
| | | 100,400,600 | 9.3177989215D-06 |

Table 4: Convergence errors were calculated for different directions and constant distance, a reflectivity value of $\rho = 0.004$, a boundary function degree $NDEG = 5$, $NINTE = 8$, and $NINTI = 32$. Various Spherical Quatrefoil ratios were tested for optimal convergence error

| Coefficient Ratio | Points (X,Y,Z) | Absolute Error |
|-------------------|----------------|------------------|
| 1:1.5:1 | -5,0,10 | 3.2607636949D-03 |
| | 0,-5,10 | 3.2607716800D-03 |
| | 5,10,0 | 3.2607473179D-03 |
| | -10,5,0 | 3.2606268804D-03 |
| 1:2:1 | -5,0,10 | 1.9237180072D-04 |
| | 0,-5,10 | 1.9237844223D-04 |
| | 5,10,0 | 1.9235549188D-04 |
| | -10,5,0 | 1.9219861537D-04 |
| 1:2.5:1 | -5,0,10 | 1.3786293525D-03 |
| | 0,-5,10 | 1.3786236565D-03 |
| | 5,10,0 | 1.3786464465D-03 |
| | -10,5,0 | 1.3788404698D-03 |

In addition to the parameters of approximating the solution of the Radiosity integral equation for the Spherical Quatrefoil, it is also possible to optimize the coefficients of the shape. As seen in the parametric equation of the Spherical Quatrefoil, the original shape has a coefficient ratio of 1:1:1. Changing this ratio alters the form of the Spherical Quatrefoil. Maple software was used to visualize the form to show that coefficients altered not only the dimensions of the shape, but that it also altered the shape's boundaries. For the reason of maintaining continuity and simply-connectedness, only the coefficient of the second parametric equation was altered. Table 4 shows a new set of simulations that allowed for optimizing coefficients of the Spherical Quatrefoil to a 1:2:1 ratio which is used for the proceeding simulations. A different set of ar-

bitrary points were used to show that a ratio diverging from a 1:2:1 ratio results in larger absolute errors.

For the purposes of optimizing the parameters of the program, distance and reflectivity are arbitrary. It should be noted that for all these simulations, different directions and varying or constant distances had little impact on the consistency of the convergence results. This could be attributed to the fact that the Spherical Quatrefoil is bilaterally symmetrical and does not prescribe a specific orientation. We will need to investigate reflectivity values in more detail. These results determine the parameters for simulation in Case 1 and 2 where $NDEG = 5$, $NINTE = 8$, $NINTI = 32$, and a Spherical Quatrefoil ratio of 1 : 2 : 1 are used.

3.2 Numerical Results for Case 1

The following data are numerical results generated for the harnessing of sunlight, an external source at a distance to the Spherical Quatrefoil. Arbitrary points which are far from the boundary of the Spherical Quatrefoil were chosen to simulate these conditions.

True functions were calculated with wavelength values ranging from 625 nm to 659 nm on the visible light spectrum to produce 2.18×10^{-15} as wave number and 3.92×10^{-6} as angular frequency. Reflectivity was chosen arbitrarily small and distance can be classified in kilometers since this scenario focused on a far away light source. Both sine and cosine were used to create emissivity functions and varying amplitudes were chosen to optimize convergence results. Amplitude values were used to detect the smallest absolute error. Varying points with the same distance but different directions were chosen. Amplitude ranges were narrowed down for each emissivity function. Absolute error as small as 10^{-6} was consistently generated in the program. Table 5 displays optimal amplitudes found for true functions in Case 1. The true emissivity functions tested are as follows,

$$U_1 = 3\cos(2.18 \times 10^{-15}X + 3.92 \times 10^{-6}Y)$$

$$U_2 = 3.05\cos(2.18 \times 10^{-15}X + 3.92 \times 10^{-6}Y)$$

$$U_3 = 0.0003\sin(2.18 \times 10^{-15}X + 3.92 \times 10^{-6}Y)$$

$$U_4 = 0.00003\sin(2.18 \times 10^{-15}X + 3.92 \times 10^{-6}Y)$$

The plotted convergence results for smallest absolute error of sinusoidal and cosinusoidal oscillating true functions are displayed in figure 6-9. While the four different points measure the same distance, their signs indicate various directions from the origin of the Spherical Quatrefoil. It is evident that the change in direction has a minor effect on the convergence results. The lower amplitude bound cosine and sine true functions (U_1 and U_4) generate a similar pattern with absolute errors identical to the tenths place. The upper amplitude bound of the cosine true function (U_2) is shown to be the most optimal result for Case 1. The plotted points of the sine true function's absolute error oscillate more than that of the cosine true

Table 5: Optimal amplitudes of different points for the true functions with wavelengths ranging from 625 nm to 659 nm of visible light. 2.18×10^{-15} as the wave number and 3.92×10^{-6} as the angular frequency, $\rho = 0.10$, $NDEG = 5$, $NINTI = 32$, $NINTE = 8$, and the coefficient ratio of 1:2:1 for the Spherical Quatrefoil.

| Emissivity Function | Amplitude | Points (X,Y,Z) | Absolute Error |
|---------------------|-----------|----------------|------------------|
| cosine | 3.05 | -100,-200,300 | 4.8864749194D-06 |
| | | 100,-200,-300 | 4.8867038855D-06 |
| | | -100,-200,-300 | 4.8863347009D-06 |
| | | 100,200,-300 | 4.8866866051D-06 |
| sine | 0.00003 | -100,-200,300 | 5.5883259517D-06 |
| | | 100,-200,-300 | 5.5883259514D-06 |
| | | -100,-200,-300 | 5.5883259519D-06 |
| | | 100,200,-300 | 6.0587259168D-06 |

function. The upper amplitude bound of the sine function suggests a decreasing linear pattern for the arbitrarily chosen points. The optimal range of amplitude for the sine function model is between [0.0003-0.00003] (Table 5). Thus, this function produces the best convergence when the light waves have small amplitudes, which occurs when there is low energy. On the contrary, the optimal range of amplitude for the cosine function model is between [3-3.05] (Table 5). In other words, results are better when light waves are more intense at higher amplitudes. Input of amplitudes outside of these ranges give significantly worse convergence results.

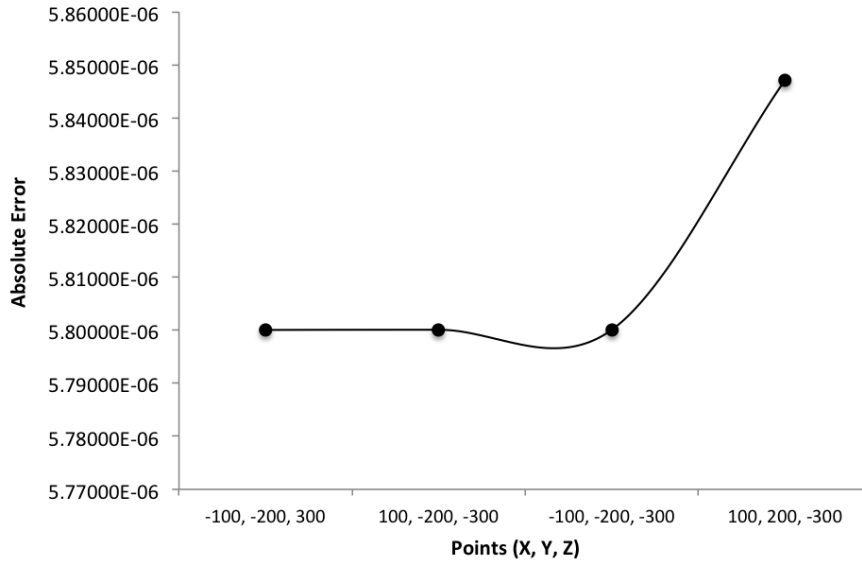


Figure 6: Convergence results for different points for the true function of $U_1 = 3\cos(2.18 \times 10^{-15}X + 3.92 \times 10^{-6}Y)$. A wave number 2.18×10^{-15} , an angular frequency 3.92×10^{-6} , $\rho = 0.10$, $NDEG = 5$, $NINTI = 32$, $NINTE = 8$, and a coefficient ratio of 1 : 2 : 1 for the Spherical Quatrefoil was used.

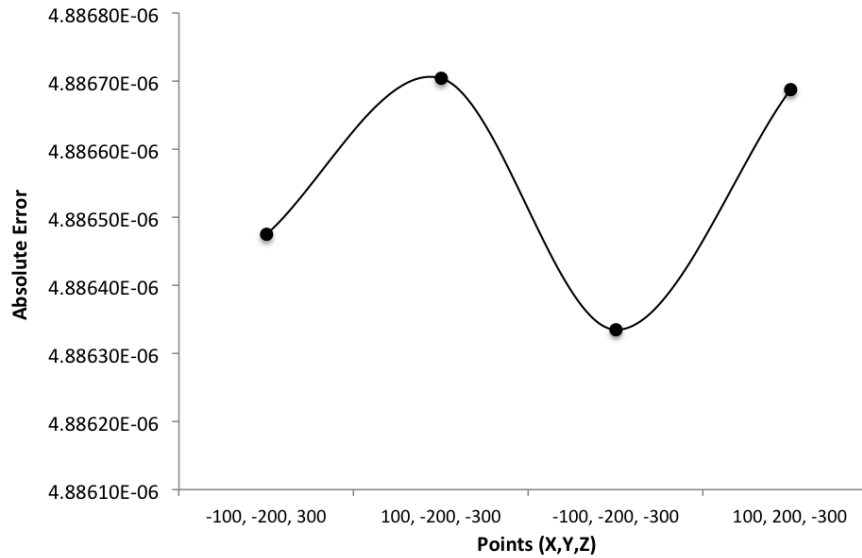


Figure 7: Convergence results for different points for the true function of $U_2 = 3.05\cos(2.18 \times 10^{-15}X + 3.92 \times 10^{-6}Y)$. A wave number 2.18×10^{-15} , an angular frequency was 3.92×10^{-6} , $\rho = 0.10$, $NDEG = 5$, $NINTI = 32$, $NINTE = 8$, and a coefficient ratio of 1 : 2 : 1 for the Spherical Quatrefoil was used.

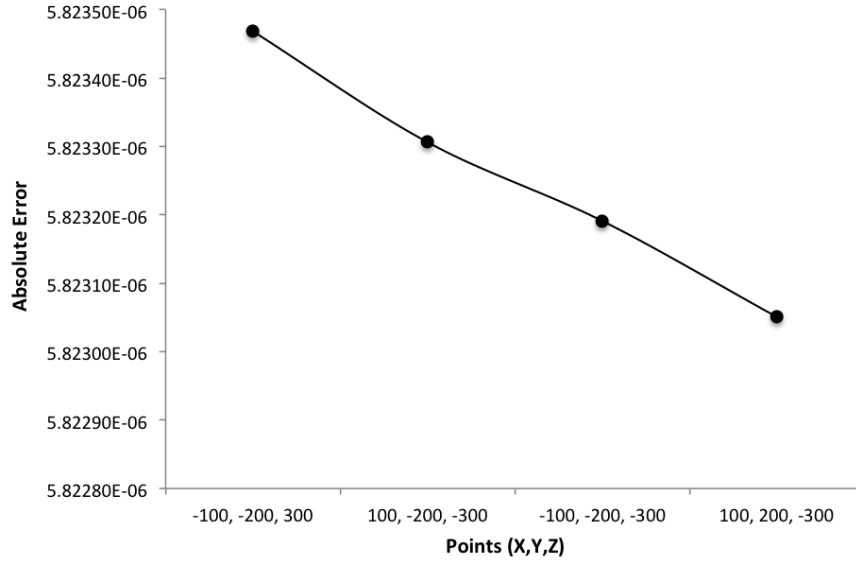


Figure 8: Convergence results for different points for the true function of $U_3 = 0.0003\sin(2.18 \times 10^{-15}X + 3.92 \times 10^{-6}Y)$. A wave number 2.18×10^{-15} , an angular frequency was 3.92×10^{-6} , $\rho = 0.10$, $NDEG = 5$, $NINTI = 32$, $NINTE = 8$, and a coefficient ratio of 1 : 2 : 1 for the Spherical Quatrefoil was used.

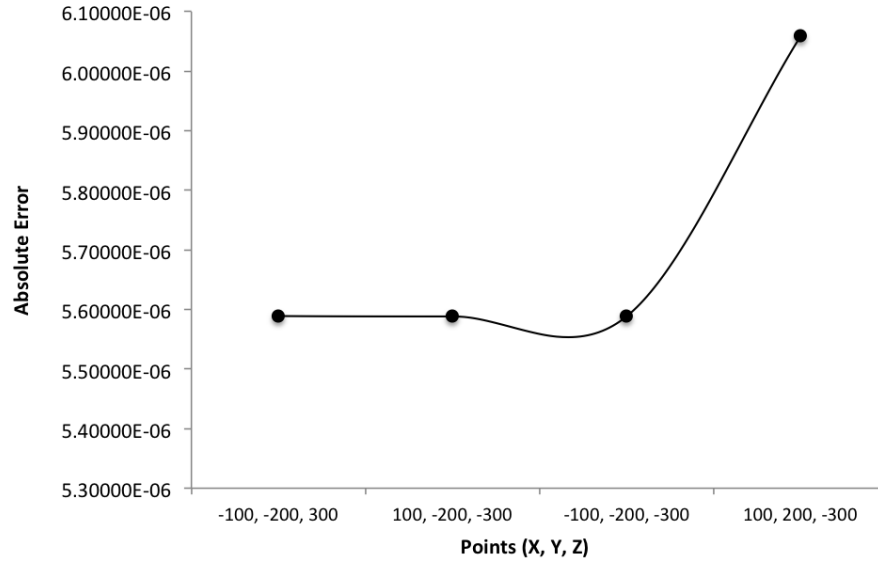


Figure 9: Convergence results for different points for the true function of $U_4 = 0.00003\sin(2.18 \times 10^{-15}X + 3.92 \times 10^{-6}Y)$. The wave number was 2.18×10^{-15} , the angular frequency was 3.92×10^{-6} , $\rho = 0.10$, $NDEG = 5$, $NINTI = 32$, $NINTE = 8$, and a coefficient ratio of 1 : 2 : 1 for the Spherical Quatrefoil was used.

The above graphs are plotted equidistant from the Spherical Quatrefoil. Even with these various observed trends, the amplitude (energy level) of the emissivity function has a small effect on overall convergence results using our standards of error tolerance. This implies that the direction of the sunlight would have a small impact on overall numerical convergence.

3.3 Numerical Results for Case 2

This section presents numerical results generated for brightness derived from an internal artificial light source. The light source must technically reside on the exterior of the Spherical Quatrefoil in order for us to hold the integrity of our Radiosity Integral Equation model and its prescribed conditions. In this case, we use points that measure smaller distances and classify our units in terms of meters. The dimensions taken from the mapping of the Spherical Quatrefoil will denote the minimum distance that we will run simulations with. True functions were calculated with wavelength values ranging from 455 nm to 492 nm on the visible light spectrum to produce 1.58×10^{-15} as a wave number and 4.72×10^{-21} as angular frequency. Firstly, various amplitude values were tested with arbitrarily small reflectivity values.

Table 6: Convergence results for blue emissivity sine function. Emissivity was given by $U = A \sin(1.58 \times 10^{-15} X - 4.72 \times 10^{-21} Y)$. A coefficient ratio of 1:2:1 for the Spherical Quatrefoil and $\rho = 0.004$ was used. NDEG=5, NINTI=32, and NINTE=8. From 4 different directions, 4 different amplitudes (1,2,5 and 10) were tested and 1 and 10 showed to be the most viable.

| Amplitude (A) | Distance | Points (X,Y,Z) | Absolute Error |
|---------------|-----------|----------------|------------------|
| 1 | 11.18034 | 0,5,10 | 9.3177830568D-06 |
| | 12.529964 | 0,6,11 | 9.3177830515D-06 |
| | 13.892444 | 0,7,12 | 9.3177830515D-06 |
| | 15.264338 | 0,8,13 | 9.3177830515D-06 |
| 10 | 11.18034 | 0,5,10 | 9.3177828362D-06 |
| | 12.529964 | 0,6,11 | 9.3177828309D-06 |
| | 13.892444 | 0,7,12 | 9.3177828305D-06 |
| | 15.264338 | 0,8,13 | 9.3177828302D-06 |

With varying energy levels used as inputs for the program, differences in absolute error are extremely small and do not occur until the last five decimal places. Comparing these different absolute errors show that higher amplitudes result in more optimal convergence.

We next observe the differences in emissivity true functions using sine and cosine functions. The plotted convergence results present mirrored directional patterns at the same points (Figure 11). It was found that the sine emissivity true function ultimately produces lower absolute error (Figure 10).

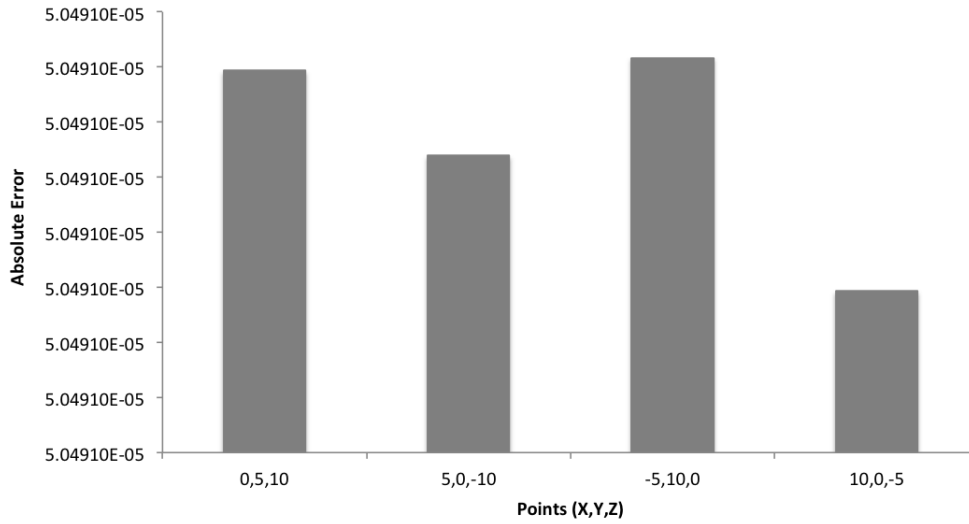


Figure 10: Convergence results for blue emissivity sine function. Emissivity given by $U = \sin(1.58 \times 10^{-15}X - 4.72 \times 10^{-21}Y)$. A coefficient ratio of 1 : 2 : 1 for the Spherical Quatrefoil and $\rho = 0.004$ was used. $NDEG = 5$, $NINTI = 32$, and $NINTE = 8$. Four different directions of the same distance were used.

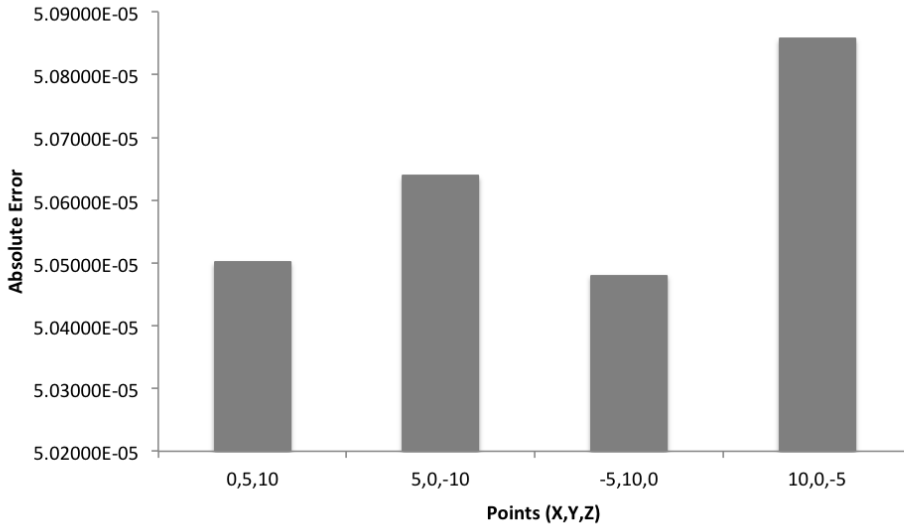


Figure 11: Convergence results for blue emissivity sine function. Emissivity given by $U = \cos(1.58 \times 10^{-15}X - 4.72 \times 10^{-21}Y)$. A coefficient ratio of 1 : 2 : 1 for the Spherical Quatrefoil and $\rho = 0.004$ was used. $NDEG = 5$, $NINTI = 32$, and $NINTE = 8$. Four different directions of the same distance were used.

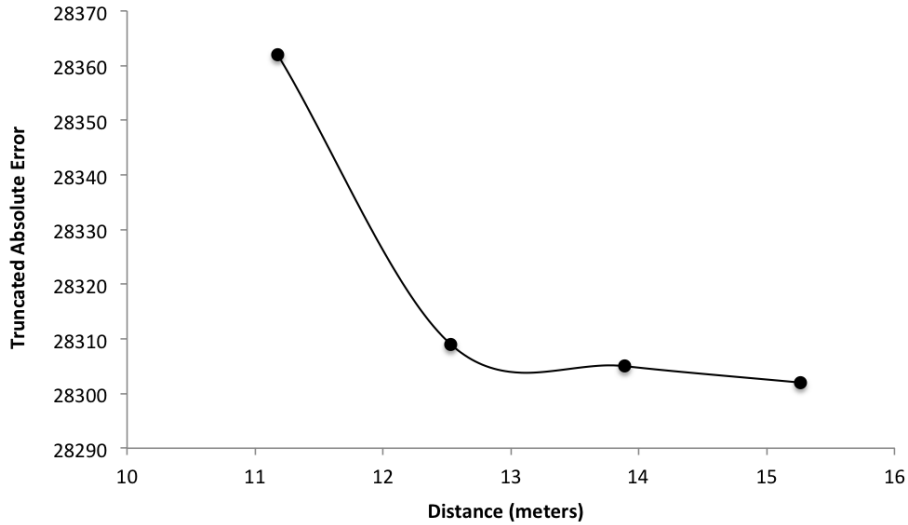


Figure 12: Optimal convergence results for blue light emissivity function of a sine function for various points using an amplitude of 10; emissivity given by $U_5 = 10\sin(1.58 \times 10^{-15} - 4.72 \times 10^{-21}Y)$, $\rho = 0.004$, and a coefficient ratio of 1 : 2 : 1 for the Spherical Quatrefoil was used. $NDEG = 5$, $NINTI = 32$, and $NINTE = 8$. Four different points with increasing distance from the boundary of the shape were used. Values of absolute error have been truncated for scaling of identifying differences.

For our next simulation we incorporate both the sine function and a high amplitude into the emissivity true function. Points further away from the boundary converge with less error than those which are closer to the boundary. This could be attributed to the fact that the integrand is mathematically more singular at points near the boundary. In other words, optimal solutions are found as the point of light source is positioned further away from the Spherical Quatrefoil away from the boundary.

A closer light source entailed a more detailed understanding of the space and its reflectivity. The Spherical Quatrefoil in Case 2 will be thought of as a module that only contains a work station and seats. We have simplified the structure to build a network of weighted emissivity averages to optimize overall reflectivity. Using the emissivity sine true function from the previous simulations, the convergence results of various reflectivities (ρ) are generated and presented in Table 7. Weighted averages of various components were used as preliminary guides for testing reflectivity. These weighted averages accounted for published emissivity values of materials and the percentage of the total area (Table 1). The inverse relationship between emissivity and reflectivity was then used to find the relative reflectivity for the entirety of the Spherical Quatrefoil. Figure 13 illustrates the effects of increasing diffuse reflection for the minimum distance for optimal brightness. Convergence results reveal that absolute error increases with higher dif-

fuse reflection. In solving the Radiosity Integral Equation for the Galerkin Method, one of our assumptions is that we use Lambertian diffuse reflectors. These results confirm that unequal luminance from different directions cause worse convergence results.

Table 7: Convergence results for blue emissivity sine function. Emissivity was given by $U_5 = 10\sin(1.58 \times 10^{-15}X - 4.72 \times 10^{-21}Y)$. A coefficient ratio of 1:2:1 for the Spherical Quatrefoil, $NDEG = 5$, $NINTI = 32$, and $NINTE = 8$ were used. Various diffuse reflectivity values were tested. Points are listed and their distances are 11.18034, 12.569805, 44.877611, and 134.632834 respectively.

| Reflectivity | Diffuse Reflection | Points (X,Y,Z) | Absolute Error |
|--------------|--------------------|----------------|------------------|
| 0.016125 | 0.01 | 0,5,10 | 9.8210003324D-06 |
| | | 1,6,11 | 9.8211583726D-06 |
| | | 5,30,33 | 9.8217905567D-06 |
| | | 15,90,99 | 9.8233705558D-06 |
| 0.047417 | 0.06 | 0,5,10 | 2.8879371616D-05 |
| | | 1,6,11 | 2.8879529964D-05 |
| | | 5,30,33 | 2.8880163557D-05 |
| | | 15,90,99 | 2.8881741475D-05 |
| 0.013625 | 0.005 | 0,5,10 | 8.2983843048D-06 |
| | | 1,6,11 | 8.2983859136D-06 |
| | | 5,30,33 | 8.2983923651D-06 |
| | | 15,90,99 | 8.2984081647D-06 |

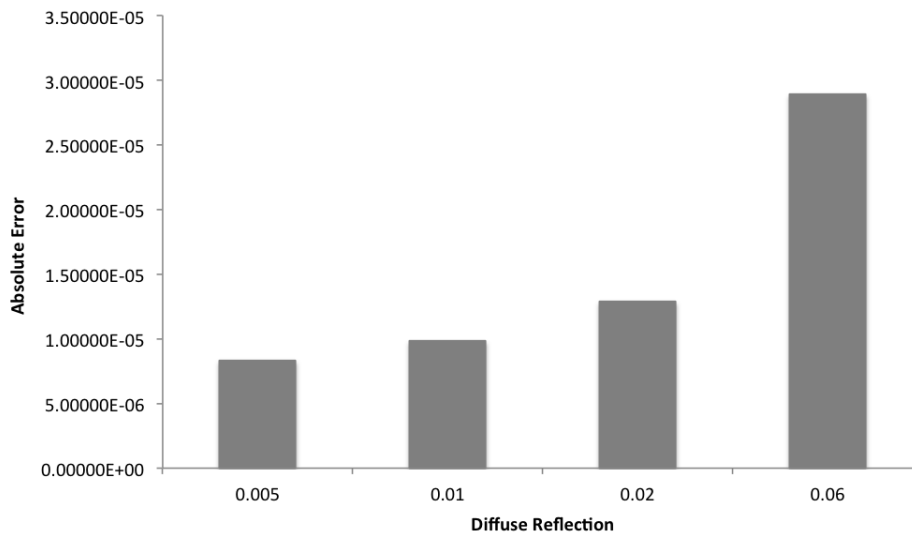


Figure 13: Convergence results for blue emissivity sine function. Emissivity given by $U = 10\sin(1.58 \times 10^{-15}X - 4.72 \times 10^{-21}Y)$, and a coefficient ratio of 1 : 2 : 1 for the Spherical Quatrefoil and a distance of 11.8034 was used. $NDEG = 5$, $NINTI = 32$, and $NINTE = 8$. Various diffuse reflectance values were used in the calculation of reflectivity.

Table 8: Convergence results for blue emissivity sine function. Emissivity given by $U = 10\sin(1.58 \times 10^{-15}X - 4.72 \times 10^{-21}Y)$. A coefficient ratio of 1 : 2 : 1 for the Spherical Quatrefoil and a $\rho = 0.013625$ was used. NDEG=5, NINTI=32, and NINTE=20. Various points with increasing distance were used to evaluate optimal location of light source relative to the exterior boundary.

| Direction | Points (X,Y,Z) | Absolute Error |
|------------|----------------|------------------|
| Top | 0,0,5 | 8.2983843177D-06 |
| | 0,0,10 | 8.2983843126D-06 |
| | 0,0,30 | 8.2983843160D-06 |
| | 0,0,200 | 8.2983843175D-06 |
| Left | 0,5,0 | 8.2983843193D-06 |
| | 0,10,0 | 8.2983843198D-06 |
| | 0,30,0 | 8.2983843197D-06 |
| | 0,200,0 | 8.2983843196D-06 |
| Bottom | 0,0,-5 | 8.2983843206D-06 |
| | 0,0,-10 | 8.2983843256D-06 |
| | 0,0,-30 | 8.2983843223D-06 |
| | 0,0,-200 | 8.2983843208D-06 |
| In Between | 0,5,10 | 8.2983910873D-06 |
| | 1,6,11 | 8.2983997726D-06 |
| | 5,30,33 | 8.2984036455D-06 |
| | 15,90,99 | 8.2983927978D-06 |

For reflectivity, the simulation using $\rho = 0.013625$ consistently produced the lowest absolute error. With the proper emissivity and reflectivity function it was possible to investigate the direction for Case 2. Keeping the same distances, we varied the direction of the points (Table 8). Overall, convergence results show very small absolute error for all different directions (top, left, bottom, and in between). There is no predetermined orientation of the Spherical Quatrefoil.

In comparing all decimal places, a light source from the top vertical node of the Spherical Quatrefoil seems not only practical, but also renders the best convergence results. This will allow for maximum illumination as the light would propagate directly onto the workstation and all around to the perimeter of the horizontal node of the space capsule.

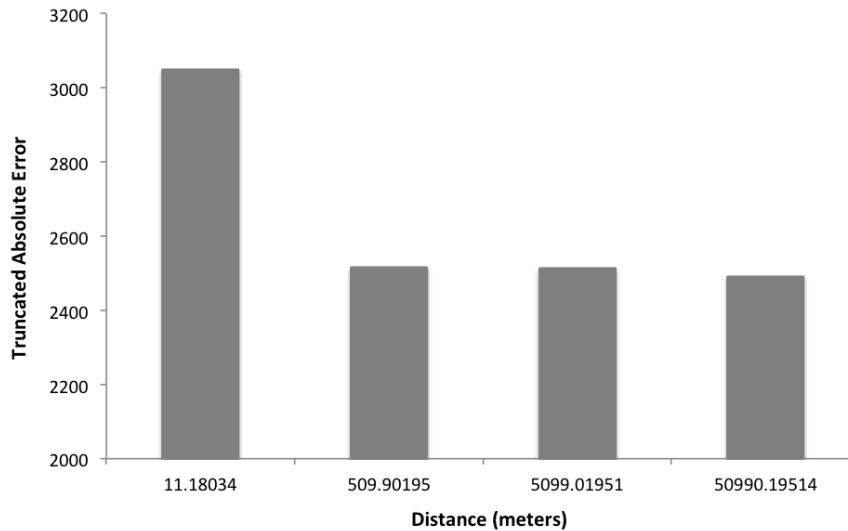


Figure 14: Convergence results for blue emissivity sine function. Emissivity given by $U = 10\sin(1.58 \times 10^{-15}X - 4.72 \times 10^{-21}Y)$, $\rho = 0.013625$, and a coefficient ratio of 0.95 : 2.07 : 1 for the Spherical Quatrefoil was used. $NDEG = 5$, $NINTI = 32$, and $NINTE = 8$. This simulation utilizes optimal amplitude, diffuse reflectivity, various points with increasing distance with the source positioned from the top relative to the exterior boundary.

Case 2 prescribes that we have an artificial light source that is close to the boundary of the surface. It is evident that the first increment of increasing distance shows the most change in absolute error. Therefore if there is a way to alter the circumstance of the light source’s location, then even better convergence results could be rendered. This may entail a scenario different from Case 1 and Case 2.

In the process of running simulations for case 2, it was necessary to simultaneously optimize parameters within the program. For example, the ratio of the Spherical Quatrefoil was slightly changed from 1 : 2 : 1 to 0.95 : 2.07 : 1 to render better convergence results. This shows that the model is very sensitive to slight changes in both parameters and inputs of the program. The nature of numerical analysis allows for the identification of those sensitivities. These are important notions in understanding the various factors involved in the Radiosity Integral Equation model as well as implications for its application.

All calculations of absolute error came from Fortran 77. We conclude that convergence results or error is affected by the boundary, boundary data, emissivity, reflectivity, and the position of the light source. In these cases we believe that we found the optimal solutions for the number of integration nodes that were used in calculating Galerkin coefficients $(h_i, \hat{K}h_j)$.

4 Discussion

This research was conducted in an effort to provide insight on brightness and illumination for spacecraft designs using mathematical models and computational simulations. Optimizing Radiosity contributes to a higher quality of living and supports human productivity. Appropriate structure and resultant brightness are critical elements for future long-term manned missions beyond Earth.

Overall, an exterior light source far from the boundary of the Spherical Quatrefoil for the Radiosity integral equation model results in small absolute errors. Convergence results generated for various combinations of interior reflectivity and emissivity were found to be viable in this case of harnessing light from the sun. This allowed for several ideas in designing the interior of the Spherical Quatrefoil. If the structure were to be scaled large enough, there could be enough room for a control systems, work stations, and even recreation. While space capsules are typically smaller than 5 meters there is no engineering limit to larger sizes. In our research, the interior design was first simplified to investigate a volumetrically efficient and structurally strong design encapsulating brightness and Radiosity.

The Spherical Quatrefoil was investigated with the intentions to contain and transport humans for some duration of a Mars mission. In theory, crew members would spend time both working and resting in the spacecraft. The habitat could be similar to the Orion Multi-Purpose Crew Vehicle (Orion MPCV) which is intended to carry a crew of four astronauts both to and beyond the low Earth orbit. NASA used a separate vehicle called the Deep Space Habitat which is designed to support long-duration deep space missions. This habitat would contain life support, propulsion, thermal protection, and avionics systems [15]. Furthermore, the Spherical Quatrefoil could potentially serve as either a habitat or a vehicle.

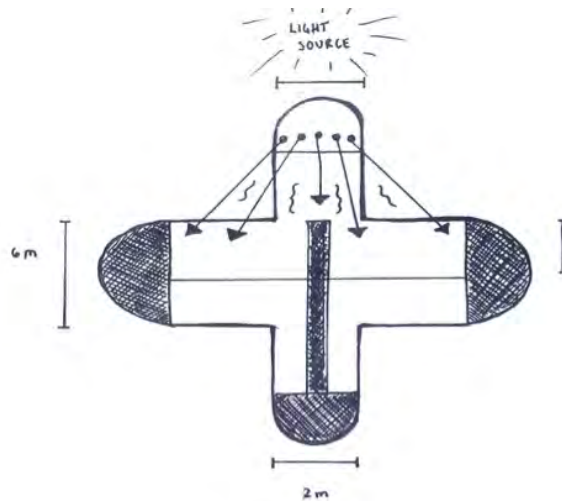


Figure 15: A preliminary sketch of the Spherical Quatrefoil and its interior configuration with its original ratio of 1:1:1.

4.1 Thermal Control

Since reflectivity is an optical property that depends on emissivity, the potential effects of what materials used within the interior of the spacecraft need to be considered if humans are to inhabit it. In addition, it is necessary to have a system of thermal control suitable for human habitation. The temperature inside the International Space Station (ISS) without thermal controls, would vary from 121 C to -157 C depending on whether the station is facing the sun or not. Within the ISS, a highly reflective material called Multi-Layer Insulation (MLI) made of Mylar and Dacron shields the space station from radiation while also preventing the extremely cold temperatures of space from penetrating the station. In addition to insulation, engineers, and designers of the ISS created the Active Thermal Control System (ATCS), which allows for excess heat within the spacecraft to be released. Excess heat is removed through cold plates and heat exchangers which cool and dehumidify the internal atmosphere of the spacecraft. There is also the Environmental Control and Life Support System (ECLSS) that controls the air quality and flow within the station [19]. This is needed in the orbiting free-fall conditions of outer space, however it may be adjusted or modified for habitation on Mars considering the existence of gravity on Mars. Furthermore, there are many designs and engineering systems that have been created in efforts to help create comfortable habitable conditions within the ISS, and they can thus be used for a habitat on Mars.

4.2 Design of Spherical Quatrefoil

Radiosity varies with the type of materials that are used and a surface's micro structure defines both reflectivity and emissivity. In these simulations, the Dirichlet condition for the Radiosity integral equation is applied and it is assumed that only Lambertian surfaces are involved. Case 2 incorporates matte surfaces with high emissivities to compute weighted averages between all the surfaces. For the purposes of our research, we tested for various ranges to optimize convergence absolute error results.

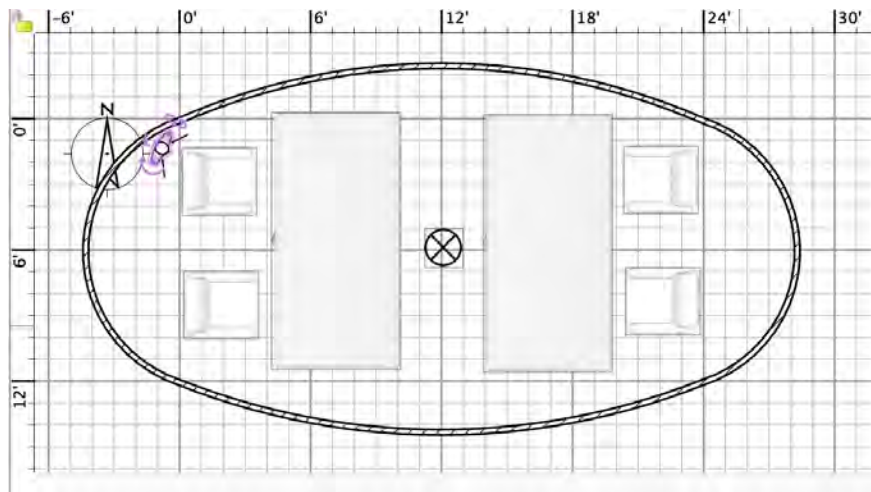


Figure 16: Updated layout of interior space capsule consisting of basic workstation panels and controlling system consoles on both ends surrounding four seats mapped and drawn out.

Preliminary calculations of the Spherical Quatrefoil's dimensions allowed for a design with considerations for individuals to occupy the space for a long period of time. The habitat has been drawn out with the consideration that there could be enough room to sustain the habitual lifestyle of four crew members. There are necessities such as beds, showers, restrooms, a kitchen area, a workstation, and amenities. In accordance with the goal to model lighting inside the space, it needed to be simple and manageable in diagramming and calculating emissivity. The most basic components with calculable emissivity and reflectivity indexes; walls, floors, ceilings, couches, workstation, kitchen, and dining were taken. The units of each of these components have been measured in correspondence to real-life dimensions of walls, and furniture pieces. The projected room for empty space is maximized for comfort and psychological consideration. The materials that have been chosen for the construction of each of the components are based on purpose and efficiency while having been laboratory-tested and authorized by NASA.

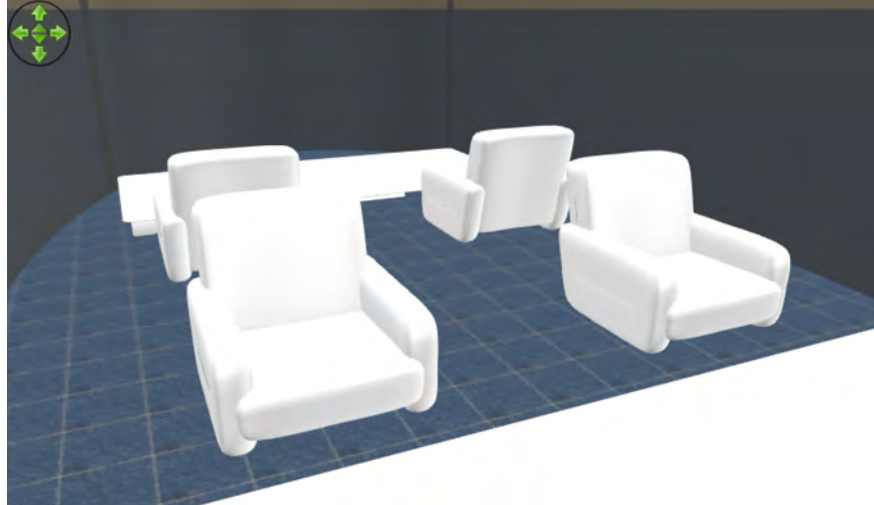


Figure 17: Perspective of interior arrangement from a stored point of view with mocked Martian sky and blue light flooring.

Exploring Case 2 led to modifications of the original arrangement inside the Spherical Quatrefoil. Instead of an independent spacecraft, this scenario posits that the form is an interior space within a larger spacecraft. The composition of the interior was designed to maintain principles of balance and symmetry. The space has been drawn out with the consideration that there could be enough room to sustain the life of four crew members (Figure 16). As a workstation with minimal amenities, the room could be similar to the prototypes of space ascent vehicles. It should be noted that Case 1 assumes that sunlight could be harnessed most practically from the uppermost vertical node of the Spherical Quatrefoil. Generating convergence results from Case 2 confirmed that this position of an artificial light source would provide maximum brightness and light exposure to and from all other parts within the habitat. It was also found that the symmetrical nature of the Spherical Quatrefoil allows for arbitrary light positions and directions, and thus orientation. This is important because it implies that the Spherical Quatrefoil form shows a range of versatility and the ability to be scaled and modified accordingly.

Through simulations for convergence error of various points from the boundary and outside of the boundary, it was found that positioning a light source from any direction generated absolute error less than 10^{-5} . For our design, the light source is positioned directly above the center in the top protruding node as humans to emulate what humans are accustomed to on planet Earth. The layout of the workstation surrounding the seats were inverted so that brightness would be concentrated on those panels and

consoles for the purposes of working. Reviewed literature informed our decision to model Case 2 with reflectivity and emissivity indexes of blue light. It has been found that color is a element that has the ability to affect the melatonin production of the brain which has the ability to influence alertness and sleepiness. More specifically, research has reported that blue light has strong impacts on dinoflagellates and can be greatly efficient in maintaining synchronized circadian rhythms [11]. Our numerical convergence results support our design for an internal artificial light source along with the selected materials and the arrangement within the Spherical Quatrefoil.

The habitat's parametric quantities provide conditions for theoretical designs. Published data on material surfaces enable detailed simulations on illumination and brightness within the habitat.. Laboratory-tested structures and materials with reported total emissivity measurements for metals, non-metals and common building materials were used to select reflectivity inputs for simulations of brightness. Since emissivity of materials vary as functions of temperature, it will be necessary to derive functions that model the oscillation of light waves on the interior of the Spherical Quatrefoil using emissivity functions rather than constant values. Various emissivity functions, reflectivity inputs, degrees of boundary functions, interior and exterior integration nodes, designated distance points chosen within the Radiosity equation model and their compatibility with the Spherical Quatrefoil will be simulated. Methods that model and generate low absolute error or successful convergence results gave rise to specific designs for proper illumination of a habitat that can ultimately be used for future endeavors in Mars exploration.

4.3 Rendering of Visual Model

Lighting is a very complex aspect in the rendering process. There has not yet been a "perfect" simulation of rendering for use in real-time or non-real-time graphics for every material. Sweet home 3D is an interior design application with an interface allowing for a floor plan and a 3D preview of the Spherical Quatrefoil's interior space [23]. This application was used to create model images of how the interior of the Spherical Quatrefoil might look. In addition, a 3-D printed model of the Spherical Quatrefoil was considered. However, this research is focused on modeling the illumination of an interior space. Truly visualizing the results of our simulations require a mock-up of that interior space on a larger scale than a printed form.

Fortunately, there are Industrial design students at the Rhode Island School of Design who have created full-scale mock-ups of Mars Ascent Vehicles (MAV). They have generously donated one of their mock-ups for the purpose of a visual aid in this research. The MAV while is not in the form of the Spherical Quatrefoil provides an opportunity to visualize the resulting design of an interior space. The mock-up itself exists in the form of a spherical pod. It was necessary to install certain characteristics that resonate with our model. For instance, being simply-connected and smooth on the exterior is one of the essential reasons why the solution to the Radiosity integral equation model can be numerically approximated. Of all the materials considered for this task, paper was the most malleable and cost-effective in achieving a smooth and continuous surface. This process was done over the course of several stages and was documented in Figure 19.

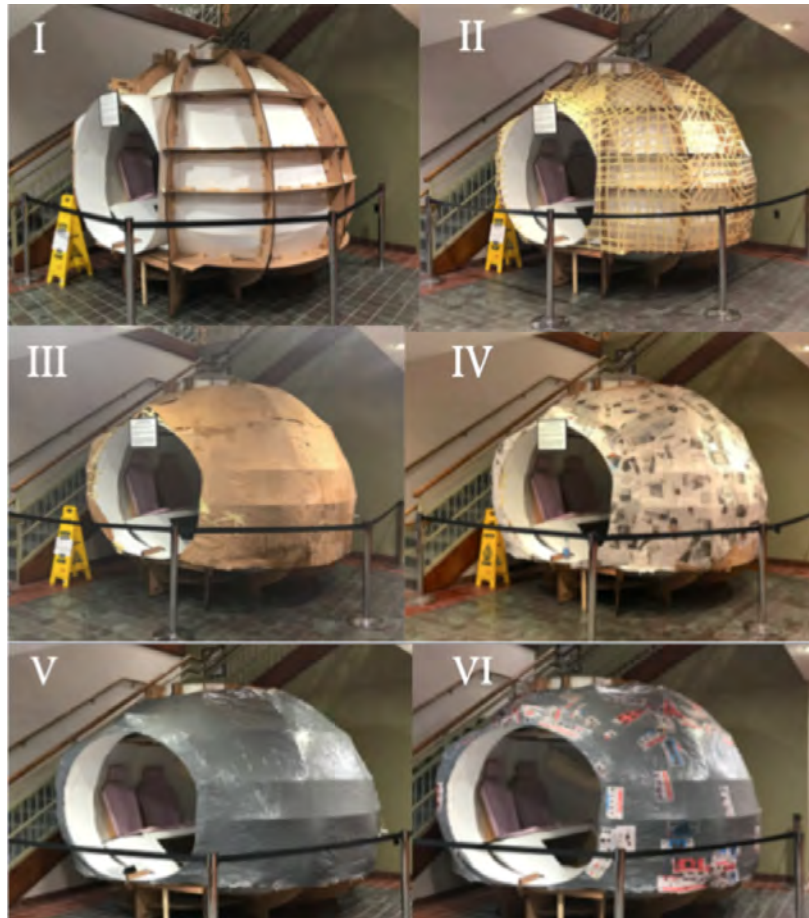


Figure 18: Phases I-IV of MAV Case 1 and Case 2 installations over the course of 65 hours.

In addition to fulfilling Green's Theorem, it was necessary to model the resulting details of Case 2 with an artificial blue light source among colors and materials of the furniture on the inside. Blue gel shades were installed in addition to remote blue LED lights to create our light source. The walls and furniture were painted to simulate the convergence results found from investigating Case 2 (Figure 20).



Figure 19: Interior of MAV simulates design for numerical results of Case 2 Brightness from an internal artificial light source.

4.4 Future Direction

Throughout the investigation of Case 1 and 2, $NDEG = 5$ was found to be optimal and used throughout this research. This degree was achieved with a program running on 26 sets of nodes and weights. Recently, the Keisan Online Calculator service provided by Casio Computer Co., Ltd., which carries out high accuracy calculations for up to 100 sets of nodes and weights of Gaussian Quadrature, was discovered [13]. The calculator uses the method of Legendre polynomials given by,

$$\int_{-1}^1 f(x)dx \simeq \sum_{i=1}^n w_i f(x_i)$$

where nodes x_i : the i -th zeros of $P_n(x)$ and weights are

$$w_i = \frac{2(1 - x_i^2)}{[nP_{n-1}(x_i)]^2} = \frac{2}{P_n^1(x_i)]^2}.$$

The implementation of these nodes and weights required diagnostic and troubleshooting simulations. The program is sensitive and so it was necessary to ensure that simulation results were generated from the newly inputted nodes or weights and not from coding errors.

It was hypothesized that increasing Gaussian Quadrature nodes and weights in the program would allow for approximating the double integral with double sums more efficiently than before. Increasing the amount of nodes and weights permit smaller horizontal and vertical subdivisions of the Spherical Quatrefoil for better precision and accuracy in generating absolute errors and convergence results. After adding 14 more sets of nodes and weights, the program was run for $NDEG = 7, 11, 13$. Convergence results were generated with arbitrary points and resulted in an accuracy as small as 10^{-7} as seen in Table 9. This indicates that increasing the number of subdivisions allows for better approximations of the double integral by double sums. Future work in adding the available 60 sets of Gaussian Quadrature nodes and weights could render even more impressive accuracy.

These simulations were carried out for $\rho = 0.013625$ and the emissivity function found from Case 2. Increasing the boundary value degree to $NDEG = 13$ shows a worse absolute error than $NDEG = 11$ which might suggest that $NDEG = 11$ is the most optimal for this particular emissivity function and

reflectivity condition. However, it is also possible that there are limitations with the emissivity function and the reflectivity condition found by investigating an internal artificial light source. In order to optimize overall brightness, future work could aim to use this higher boundary value degree to optimize reflectivity and emissivity for a different interior arrangement. Changing this parameter could affect the type of light source, its direction, the materials of the surfaces, and the overall design. Not only this, but the improvement of the boundary value degree also implies that the shape of the interior Spherical Quatrefoil space can be altered and fine-tuned for optimal Radiosity.

Table 9: Convergence results for various degrees with NINTI=32, NINTE=8, and a $\rho = 0.013625$. Arbitrary points were used to show the effect of increasing NDEG to 7, 11, and 13.

| Degree (NDEG) | Points (X,Y,Z) | Absolute Error |
|---------------|----------------|------------------|
| 7 | 1,2,3 | 8.8330654665D-05 |
| | 2,3,4 | 8.8330655205D-05 |
| | 3,4,5 | 8.8330654365D-05 |
| | 4,5,6 | 8.8330657500D-05 |
| 11 | 1,2,3 | 6.5446272548D-07 |
| | 2,3,4 | 6.5446132045D-07 |
| | 3,4,5 | 6.5445980151D-07 |
| | 4,5,6 | 6.5445826212D-07 |
| 13 | 1,2,3 | 6.4055174268D-05 |
| | 2,3,4 | 6.4055173051D-05 |
| | 3,4,5 | 6.4055171598D-05 |
| | 4,5,6 | 6.4055170825D-05 |

Aside from further simulations with the Radiosity Integral equation model for the Dirichlet condition, future work will aim to incorporate other viable mathematical boundary conditions for the Spherical Quatrefoil. For instance, there is the Neumann boundary condition which assumes that all incoming light waves are reflected by the outer surface. There is also the Robin boundary condition which entails portions of light waves being absorbed and others being reflected. Improvements in mathematical boundary conditions and programmed simulation methods would consequently validate designs for human missions to planet Mars.

References

- [1] Atkinson, Kendall, and Graeme Chandler. *The collocation method for solving the radiosity equation for unoccluded surfaces*. J. Integral Equations Appl 10.3 (1998): 253-290.
- [2] Birren, Faber. *Color psychology and color therapy; a factual study of the influence of color on human life*. Pickle Partners Publishing, 2016.
- [3] Black, William Zachary, and Wolfgang Wulff. *Study of design parameters of space base and space shuttle heat rejection systems*. Georgia Institute of Technology, 1970.
- [4] Brainard G, et al. *Lighting countermeasures for sleep and circadian disruption onboard the International Space Station*. 2012 NASA Human Research Program Investigators' Workshop, Houston, TX, February 14-16, 2012.
- [5] Butler, Darrell L., and Paul M. Biner. *Preferred lighting levels: Variability among settings, behaviors, and individuals*. Environment and Behavior 19.6 (1987): 695-721.
- [6] Chellappa, Sarah Laxhmi, et al. *Non-visual effects of light on melatonin, alertness and cognitive performance: can blue-enriched light keep us alert?*. PloS one 6.1 (2011): e16429.
- [7] Cook et al., *Concepts and Applications of Finite Element Analysis* John Wiley and Sons, 1989
- [8] deGroh, Kim K., et al. *NASA Glenn research center's materials international space station experiments (MISSE 1-7)*. 2008
- [9] Harrison, Albert A., and Mary M. Connors. *Human factors in spacecraft design*. Journal of spacecraft and rockets 27.5 (1990): 478-481.
- [10] Ho, C., et al. *Mars background noise temperatures received by spacecraft antennas*. The Interplanetary Network Progress Report 42 (2002): 149.
- [11] Holzman, David C. *What's in a color? The unique human health effects of blue light*. Environment Health Perspect 118.1 (2010): A22-A27.
- [12] Kaplan, Lewis D., Janine Connes, and Pierre Connes. *Carbon monoxide in the Martian atmosphere*. The Astrophysical Journal 157 (1969): L187.
- [13] Keisan Online Calculator Service by Casio ComputerCo., Ltd
- [14] Kropinski, Mary Catherine A., and Bryan D. Quaife. *Fast integral equation methods for the modified Helmholtz equation*. Journal of Computational Physics 230.2 (2011): 425-434.
- [15] Letchworth, Gary, and Roland Schlierf. *NASA planning for orion multi-purpose crew vehicle ground operations*. Aerospace Conference, 2012 IEEE. IEEE, 2012.
- [16] Maki, J. N., et al. *The color of Mars: Spectrophotometric measurements at the Pathfinder landing site*. Journal of Geophysical Research: Planets104.E4 (1999): 8781-8794.
- [17] Maple (2015). Maplesoft, a division of Waterloo Maple Inc., Waterloo, Ontario.
- [18] Markiewicz, W. J., et al. *Optical properties of the Martian aerosols as derived from Imager for Mars Pathfinder midday sky brightness data*. Journal of Geophysical Research: Planets 104.E4 (1999): 9009-9017.
- [19] Patel, Vipul P., et al. *Development of the internal thermal control system (ITCS) for international space station (ISS)* No. 2001-01-2332. SAE Technical Paper, 2001.

- [20] Prinn, Ronald G., and Bruce Fegley Jr. *The atmospheres of Venus, Earth, and Mars: A critical comparison*. Annual review of earth and planetary sciences 15.1 (1987): 171-212.
- [21] Python Software Foundation. Python Language Reference, version 2.7. Available at <http://www.python.org>
- [22] Qianxiang, Zhou. *Review on Lighting System Design for Manned Spacecraft [J]*. China Illuminating Engineering Journal 2 (2006): 000.
- [23] Sweet Home 3-D (2017). Emmanuel Puybaret / eTeks.
- [24] Warnapala, Yajni. *Numerical Solution of the Radiosity Equation via Galerkin Method: Dirichlet Condition*. International Journal of Numerical Methods and Applications 10.2 (2013): 73.
- [25] Wheelwright, C. D., and J. R. Toole. *Spacecraft lighting systems*. Industry Applications Society Annual Meeting, 1992., Conference Record of the 1992 IEEE. IEEE, 1992.

Appendices

A Surface Area

The surface area of smooth spherical surfaces such as the Spherical Quatrefoil can be evaluated using their representation as parametric surfaces. Due to the irregular nature of the Spherical Quatrefoil, formulas of the surface areas for oblate and prolate spheroid surfaces will be used in approximation. The general triaxial ellipsoid is a quadratic surface where the semi-axes are lengths a, b, and c. In spherical coordinates:

$$\frac{r^2 \cos^2 \theta \sin^2 \phi}{a^2} + \frac{r^2 \sin^2 \theta \sin^2 \phi}{b^2} + \frac{r^2 \cos^2 \phi}{c^2} = 1$$

Lengths of two axes of an ellipsoid are assumed to be the same in classification of a spheroid. Then depending on whether $c < a$ or $c > a$, the ellipsoid can be considered either an oblate spheroid or a prolate spheroid. For the horizontal spherical body component of the Spherical Quatrefoil, the oblate spheroid will be used to approximate its surface area. The ellipticity of an oblate spheroid is defined by,

$$e_{oblate} = \sqrt{1 - \frac{c^2}{a^2}}$$

The surface area of an oblate spheroid can be computed as a surface of revolution about the z-axis, with a radius as a function of z given by,

$$S = 2\pi \int r(z) \sqrt{1 + [r'(z)]^2} dz,$$

$$r(z) = a \sqrt{1 - \frac{z^2}{c^2}}$$

The simple form is given by,

$$S = 2\pi a^2 + \pi \frac{c^2}{e} \ln \frac{(1+e)}{(1-e)}$$

Thus for the spherical component at hand, a=0.02, b=0.01, and c can be calculated using $c^2 = a^2 + b^2$ which when solved, $c = 0.0173205081$. To find e we calculate the following,

$$e = \sqrt{1 - \frac{0.0173205081^2}{0.02^2}}$$

Solving for e and substituting this value into the previous equation, the surface area of the horizontal part was solved to be $S = 0.0092283489\pi = 0.0289917132$. For the vertical spherical component of the Spherical Quatrefoil, the prolate spheroid will be used to approximate its surface area. All calculations follow the previously outlined steps except that the ellipticity of the prolate spheroid is defined by,

$$e_{prolate} = \sqrt{1 - \frac{a^2}{c^2}}$$

In addition, the inner part of the Spherical Quatrefoil overlaps with the x component and subtraction of this part is necessary as to not count it twice. In other words, for this part, $a = 0.04$, $b = 0.007$, and thus, $c = 0.0080622577$. Using the formula for a surface area with e calculated, we find that $S = 3.459603087 \times 10^{-4}$. The approximated values in these calculations have no assigned units which allows for appropriate extrapolation and scaling.

B Volume

The quantity of the space enclosed by the Spherical Quatrefoil can be approximated by integral calculus. The volume integral in spherical coordinates has the form,

$$V = \int_0^{2\pi} \int_0^\pi \int_{0.002}^{0.005} f(\rho, \theta, \phi) \rho^2 \sin \theta d\rho d\theta d\phi$$

The equation for outer edge of a sphere when radius is given as,

$$a = \sqrt{x^2 + y^2 + z^2}$$

We then derive the volume integral $f(\rho, \theta, \phi)$ from x , y , and z .

$$(0.002 + 0.003 \cos^2 2\theta) \sqrt{\sin^2 \theta \cos^2 \theta (1 + 3 \sin^2 \phi)}$$

Thus, we can find the volume by evaluating the triple integral below.

$$V = \int_0^{2\pi} \int_0^\pi \int_{0.002}^{0.005} (0.002 + 0.003 \cos^2 2\theta) \sqrt{\sin^2 \theta \cos^2 \theta (1 + 3 \sin^2 \phi)} \rho^2 \sin \theta d\rho d\theta d\phi$$

SciPy, an open source Python library used for scientific computing and technical computing, was used for numerical evaluation of this triple integral. The Spherical Quatrefoil was computed to have a volume of 2.162863×10^{-9} . There are no particular units assigned which allows for appropriate extrapolation and scaling.

```
Python 2.7.12 [Anaconda 4.1.1 (x86_64)] (default, Jul 2 2016, 17:43:17)
[GCC 4.2.1 (Based on Apple Inc. build 5658) (LLVM build 2336.11.00)] on darwin
Type "help", "copyright", "credits" or "license" for more information.
Anaconda is brought to you by Continuum Analytics.
Please check out: http://continuum.io/thanks and https://anaconda.org
>>> import scipy.integrate as integrate
>>> from numpy import sin, cos, sqrt, pi
>>> h = lambda phi, theta, rho: (0.002+0.003*cos(2*theta)**2)*sqrt(sin(theta)**2*(1+3*sin(phi)**2+cos(theta)**2))*(rho**2)*sin(theta)
>>> volume = integrate.tplquad(h, 0.002, 0.005, lambda x: 0.0, lambda x: pi, lambda x,y: 0, lambda x,y: 2*pi)
Traceback (most recent call last):
  File "<stdin>", line 1, in <module>
NameError: name 'h' is not defined
>>> h = lambda phi, theta, rho: (0.002+0.003*cos(2*theta)**2)*sqrt(sin(theta)**2*(1+3*sin(phi)**2+cos(theta)**2))*(rho**2)*sin(theta)
>>> volume = integrate.tplquad(h, 0.002, 0.005, lambda x: 0.0, lambda x: pi, lambda x,y: 0, lambda x,y: 2*pi)
>>> volume
(2.1628634577527747e-09, 1.43951546706575e-17)
>>>
```

Figure 20: Snapshot of triple integral to approximate volume in Python.

C Maxwell Equations

A set of equation that describe the way electric and magnetic fields propagate, interact, and how they can be influenced by objects. These equations show that separated charges can give rise to both electric and magnetic fields.

$$\begin{aligned}\nabla \cdot D &= \rho_v \\ \nabla \cdot B &= 0 \\ \nabla \times E &= -\frac{\partial B}{\partial t} \\ \nabla \times H &= -\frac{\partial D}{\partial t} + J\end{aligned}$$

D Volterra Integral Equations

The bases of the Volterra integral equation approach is a universal method for calculating and modeling sorption kinetics of fluid multi-component mixtures in porous media. It can be divided into the first and second kind. A linear one is represented below

$$f(t) = \int_a^t K(t, s)x(s)ds$$

where f is a given function and x is an unknown function to be solved for. A linear Volterra equation of the second kind is

$$x(t) = f(t) + \int_a^t K(t, s)x(s)ds$$

The application of these equations are also important in the area of probabilistic analysis. We known that Fredholm type equations behave more or less like boundary value problems. In comparison, Volterra equations behave more like initial value problems. Nonhomogenous Volterra integral equations of the second kind of the form

$$u(x) = f(x) + \lambda \int_0^x K(x, t)u(t)dt$$

where $K(x, t)$ is the kernel of the integral equation, and λ is a parameter. The limits of integration for the Volterra integral equations are functions of x and not constants as in Fredholm integral equations. Here, integration ranges from some fixed lower limit. In the Volterra equations, the upper limit of integration is the variable x , while in the Fredholm equations, the upper limit of integration is a fixed constant. Solving the following Volterra integral equations by using the Adomian decomposition method: Example. Consider the Volterra integral Equation

$$u(x) = 1 + \int_0^x u(t)dt$$

Here, $f(x) = 1, \lambda = 1, K(x, t) = 1$. Using the decomposition series solution and the recursive scheme to determine the components $u_n, n \geq 0$, we find,

$$\begin{aligned}u_0(x) &= 1 \\ u_1(x) &= \int_0^x u_0(t)dt = \int_0^x dt = x \\ u_2(x) &= \int_0^x u_1(t)dt = \int_0^x tdt = \frac{1}{2!}x^2\end{aligned}$$

and so on. Noting that,

$$u(x) = u_0(x) + u_1(x) + u_2(x) + \dots,$$

we can easily obtain the solution in a series form given by,

$$u(x) = 1 + x + \frac{1}{2!}x^2$$

and this converges to the closed form solution

$$u(x) = e^x$$

obtained upon using the Taylor expansion for e^x Example 2.

$$u(x) = x + \int_0^x (t-x)u(t)dt$$

We can also set,

$$u_0(x) = x$$

$$u_1(x) = \int_0^x (t-x)u_0(t)dt = \int_0^x t(t-x)dt = \frac{1}{3!}x^3,$$

$$u_2(x) = \int_0^x (t-x)u_1(t)dt = \int_0^x -\frac{1}{3!}t^3(t-x)dt = \frac{1}{5!}x^5.$$

Consequently, the solution in a series form is given by,

$$u(x) = x - \frac{1}{3!}x^3 + \frac{1}{5!}x^5 + \dots$$

and in a closed form by, $u(x) = \sin x$ obtained by using the Taylor expansion of $\sin x$. Example 3. We consider here the Volterra integral equation

$$u(x) = 6x - x^3 + \frac{1}{2} \int_0^x tu(t)dt$$

Applying the decomposition technique we find,

$$u_0(x) = 6x - x^3 u_1(x) = \frac{1}{2} \int_0^x tu_0(t)dt = \frac{1}{2} \int_0^x t(6t - t^3)dt = x^3 - \frac{1}{10}x^5,$$

$$u_2(x) = \frac{1}{2} \int_0^x tu_1(t)dt = \frac{1}{2} \int_0^x t(t^3 - \frac{1}{10}t^5)dt = \frac{1}{10}x^5 - \frac{1}{140}x^7$$

Consequently, the solution in series form is given by,

$$u(x) = (6x - x^3) + (x^3 - \frac{1}{10}x^5) + (\frac{1}{10}x^5 - \frac{1}{140}x^7) + \dots,$$

where we can easily obtain the solution in a closed form given by

$$u(x) = 6x.$$

E The Modified Decomposition Method

If we have nonlinear weakly-singular Fredholm Integral Equations in the form,

$$u(x) = f(x) + \int_0^1 \frac{1}{\sqrt{(|x-t|)}} F(u(t)) dt, \quad x \in [0, 1],$$

and is generalized by the form,

$$u(x) = f(x) + \int_0^1 \frac{1}{\sqrt{[|g(x) - g(t)|]^\alpha}} F(u(t)) dt, \quad 0 < \alpha < 1, x \in [0, 1]$$

where $F(u(t))$ is a nonlinear function of $u(t)$, such as $u^2(x)$, $u^3(x)$, $e^{u(x)}$, etc. This method introduces a slight change in the recurrence relation suggested by the Adomian method. It decomposes the data function $f(x)$ into two components $f_0(x)$ and $f_1(x)$, where only $f_0(x)$ is assigned to the zeroth solution component $u_0(x)$, and the $f_1(x)$ is added to the first component $u_1(x)$ in addition to the other terms assigned by using the standard Adomian Decomposition method. The modified decomposition method proposes a modified recurrence relation given as $u_0(x) = f_0(x)$,

$$u_1(x) = f_1(x) + \int_a^b K(x, t) A_0(t) dt$$

$$u_{n+1}(x) = f_1(x) + \int_z^b K(x, t) A_n(t) dt, n \geq 1$$

For example,

$$u(x) = \sqrt{\cos x} + 2\sqrt{|x-1|} - 2\sqrt{\sin|x|} + \int_0^{\pi/2} \frac{u^2(t)}{\sqrt{|\sin x - \sin t|}} dt$$

$f(x)$ is decomposed into two parts,

$$f_0(x) = \sqrt{\cos x}, f_1(x) = 2\sqrt{\sin|x-1|} - 2\sqrt{\sin|x|}$$

The modified recurrence relation is,

$$u_0(x) = \sqrt{\cos x}$$

$$u_1(x) = 2\sqrt{\sin|x-1|} - 2\sqrt{\sin|x|} + \int_0^{\pi/2} \frac{A_0(t)}{\sqrt{|\sin x - \sin t|}} dt = 0$$

$$u(x) = \sqrt{|\cos x|}$$

F The Adomian Decomposition Method

The solution $u(x)$ of an integral equation is expressed in a series form. The components of the $u(x)$ function can be determined in a recurrent manner. We use,

$$u_0(x) = f(x)$$

and

$$u_{n+1}(x) = \lambda \int K(x, t)u_n(t)dt, \quad n \geq 0$$

Consider the Fredholm integral equation,

$$u(x) = e^x - 1 + \int tu(t)dt.$$

It is clear that,

$$f(x) = e^x - 1, \lambda = 1, K = (x, t) = t$$

To evaluate these components, $u_0(x), u_1(x), u_2(x), \dots$ of the series solution, we use the recursive scheme to find,

$$u_0(x) = e^x - 1$$

$$U_1(X) = \int tu_0(t)dt = \int (e^t - 1)dt = \frac{1}{2}$$

$$u_2(x) = \int tu_1(t)dt = \int \frac{1}{2}tdt = \frac{1}{4}$$

and so on. We note that,

$$u(x) = u_0(x) + u_1(x) + u_2(x) + \dots,$$

we can easily obtain the solution in a series form given by,

$$u(x) = e^x - 1 + \frac{1}{2}(1 + \frac{1}{2} + \frac{1}{4} + \dots),$$

The solution can be written in a closed form given by, $u(x) = e^x$ by evaluating the sum of the infinite geometric series.

G The Direct Computation Method

An efficient traditional method for solving Fredholm integral equations of the second kind is called the direct computational method. Separable or degenerate kernels $K(x, t)$ expressed will be the focus here. Without loss of generality, it may be assumed that the kernel can be expressed as,

$$K(x, t) = g(x)h(t)$$

Accordingly, the equation becomes

$$u(x) = f(x) + \lambda g(x) \int_a^b h(t)u(t)dt$$

The definite integral in the above equation reveals that the integrand depends on one variable, namely t . This means that the definite integral is equivalent to a numerical value α , where α is a constant. In other words,

$$\alpha = \int h(t)tu(t)dt$$

It follows that the becomes,

$$u(x) = f(x) + \lambda\alpha g(x)$$

It is clear that the solution is completely determined by the above equation upon evaluating the constant α . This can be done by substitution. It is worth noting that the direct computation method determines the exact solution in a closed form, rather than a series form, provided that the constant α is evaluated. In addition, this method usually gives rise to a system of algebraic equations depending on the structure of the kernel. For example, there could be more than one constant. For linear Fredholm integral equations, we obtain one value for alpha and the linear equation has a unique solution. For example,

$$u(x) = x^2 - \frac{25}{12}x + 1 + \int xu(t)dt$$

We define constant, α

$$\alpha = \int tu(t)dt$$

Write the constant in terms of the original function,

$$\alpha = x^2 - \frac{25}{12}x + 1 + \alpha$$

Write the function in terms of variable t ,

$$u(t) = t^2 - \frac{25}{12}t + 1 + \alpha$$

Substitute alpha back into the function,

$$\alpha = \int t(t^2 - \frac{25}{12}t + 1 + \alpha)dt$$

Integrate from $[0, 1]$ to solve for α ,

$$\alpha = \int_0^1 t^3 - \frac{25}{12}t^2 + t + \alpha + \alpha t dt$$

$$\alpha = 4$$

H Finite Difference Method

The method can be used for elliptic partial differential equations. It is a numerical method that only does rectangular regions which leaves a margin for error in approximation. It is given by,

$$2\left[\left(\frac{h}{k}\right)^2 + 1\right]W_{ij} - (W_{i+1,j} + W_{i-1,j}) - \left(\frac{h}{k}\right)^2(W_{i,j+1} + W_{i,j-1}) = -h^2f(X_i, Y_i)$$

where h are horizontal subdivisions, k are vertical subdivisions, and w are weights, and $i = 1 \dots n - 1$ and $j = 1 \dots m - 1$. along with boundary conditions as follows,

$$W_{0j} = g(X_0, Y_j) \quad \text{and} \quad W_{nj} = g(X_n, Y_j) \quad \text{for} \quad j = 0 \dots m$$

$$W_{i0} = g(X_i, Y_0) \quad \text{and} \quad W_{im} = g(X_i, Y_m) \quad \text{for} \quad i = 1 \dots n - 1$$

For example, determining the steady state heat distribution in a thin square metal plane with dimensions $0.5m \times 0.5m$ using the Finite Difference method for $n = m = 4$. The adjacent boundaries held at 0° and heat on other boundary increases linearly for 0° from one corner to 100° where sides meet. We have a homogeneous, second-order, partial, differential equation.

$$\frac{\partial^2 u}{\partial x^2}(x, y) + \frac{\partial^2 u}{\partial y^2}(x, y) = 0$$

where $0 < x < 0.5$ and $0 < y < 0.5$ and the given boundary conditions are: $u(0, y) = 0$, $u(x, 0.5) = 200x$, $u(x, 0) = 0$, and $u(0.5, y) = 200y$.

$$2\left[\left(\frac{4}{4}\right)^2 + 1\right]W_{ij} - (W_{i+1,j} + W_{i-1,j}) - \left(\frac{4}{4}\right)^2(W_{i,j+1} + W_{i,j-1}) = -h^2f(X_i, Y_i)$$

where $i = 1 \dots 3$ and $j = 1 \dots 3$

$$W_{ij} = \frac{W_{i+1,j} + W_{i-1,j} + W_{i,j+1} + W_{i,j-1}}{4}$$

To find the weights:

$$W_{0j} = W_{01} = W_{02} = W_{03} = 0$$

$$W_{i0} = W_{10} = W_{20} = W_{30} = 0$$

$$W_{nj} = W_{41} = W_{14} = 200(0.125) = 25$$

$$W_{nj} = W_{24} = W_{42} = 200(0.25) = 50$$

$$W_{nj} = W_{34} = W_{43} = 200(0.375) = 75$$

Taking the points that surround each intersection on the grid made by vertical and horizontal subdivisions, we create a system of equations as follows.

$$P_1 : \quad 4W_1 - W_2 - W_4 = 25$$

$$P_2 : \quad 4W_2 - W_1 - W_3 - W_5 = 50$$

$$P_3 : \quad 4W_3 - W_2 = 150$$

$$P_4 : \quad 4W_4 - W_1 - W_5 - W_7 = 0$$

$$P_5 : \quad 4W_5 - W_2 - W_4 - W_6 - W_8 = 0$$

$$P_6 : \quad 4W_6 - W_3 - W_5 - W_9 = 50$$

$$P_7 : \quad 4W_7 - W_4 - W_8 = 0$$

$$P_8 : \quad 4W_8 - W_5 - W_7 - W_9 = 0$$

$$P_9 : 4W_9 - W_6 - W_8 = 25$$

Putting the above equations into a matrix, we obtain the weights W_n which approximate the heat distribution at the 9 points on the metal plate with the provided boundary conditions. $W_1 = 18.75$, $W_2 = 37.5$, $W_3 = 56.25$, $W_4 = 12.5$, $W_5 = 25$, $W_6 = 37.5$, $W_7 = 6.25$, $W_8 = 12.5$, and $W_9 = 18.75$.

I Legendre Polynomials

$\int_{-1}^1 P(x)P_n(x) = 0$ wherever $P(x)$ is a polynomial of degree less than n and is characteristically orthogonal. The first few Legendre Polynomials as roots are listed below:

$$\begin{aligned} P_0(x) &= 1 \\ P_1(x) &= x \\ P_2(x) &= x^2 - \frac{1}{3} \\ P_3(x) &= X^3 - \frac{3}{5}x \\ P_4(x) &= X^4 - \frac{6}{7}x^2 + \frac{3}{35} \end{aligned}$$

If $X_1 \dots X_n$ are the roots of the n^{th} Legendre polynomial $P_n(x)$, then the coefficients can be found using:

$$C_i = \int_{-1}^1 \prod_{j=1}^n \left(\frac{X - X_j}{X_i - X_j} \right) dx$$

For example, for $n = 3$ we have the following:

$$C_i = \int_{-1}^1 \left(\frac{X - X_1}{X_i - X_1} \right) \left(\frac{X - X_2}{X_i - X_2} \right) dx$$

We approximate by sums with,

$$\begin{aligned} \int_{-1}^1 P(x) dx &\approx \prod_{i=1}^n C_i f(X_i) \\ \int_{-1}^1 f(x) dx &\approx C_1 f(X_1) + C_2 f(x_2) + C_3 f(x_3) \\ \int_{-1}^1 P(x) dx &\approx \int_{-1}^1 (a_0 + a_1 X + a_2 x^2 + a_3 x^3 + a_4 x^4 + a_5 x^5) dx \end{aligned}$$

Therefore,

$$C_1 f(x_1) + c_2 f(x_2) \approx a_0 \int_{-1}^1 1 dx + a_1 \int_{-1}^1 x dx + a_2 \int_{-1}^1 x^2 dx + a_3 \int_{-1}^1 x^3 dx + a_4 \int_{-1}^1 x^4 dx + a_5 \int_{-1}^1 x^5 dx$$

After equating the coefficients and integrating, we find a system of 4 equations and can thereafter solve for both roots and coefficients using Mathematica. The system is as follows,

$$\begin{aligned} C_1 + C_2 + C_3 &= 2 \\ C_1 X_1 + C_2 x_2 + C_3 x_3 &= 0 \\ C_1 X_1^2 + C_2 x_2^2 + C_3 x_3^2 &= \frac{2}{3} \\ C_1 X_1^3 + C_2 x_2^3 + C_3 x_3^3 &= 0 \end{aligned}$$

$$C_1 X_1^4 + C_2 x_2^4 + C_3 x_3^4 = \frac{2}{5}$$

$$C_1 X_1^5 + C_2 x_2^5 + C_3 x_3^5 = 0$$

where we have a simultaneous system of 6 nonlinear equations and we solve for all coefficients C_n and roots x_n .

```
for n = 3
Solve[{a+b+c==2, a*d+b*e+c*f==0, a*d^2+b*e^2+c*f^2==2/3, a*d^3+b*e^3+c*f^3==0, a*d^4+b*e^4+c*f^4==2/5,
a*d^5+b*e^5+c*f^5==0}, {a, b, c, d, e, f}]
{{a -> 5/9, b -> 5/9, c -> 8/9, d -> sqrt(3/5), e -> -sqrt(3/5), f -> 0}, {a -> 5/9, b -> 5/9, c -> 8/9, d -> -sqrt(3/5), e -> sqrt(3/5), f -> 0},
{a -> 5/9, b -> 8/9, c -> 5/9, d -> sqrt(3/5), e -> 0, f -> -sqrt(3/5)}, {a -> 8/9, b -> 5/9, c -> 5/9, d -> 0, e -> sqrt(3/5), f -> -sqrt(3/5)},
{a -> 5/9, b -> 8/9, c -> 5/9, d -> -sqrt(3/5), e -> 0, f -> sqrt(3/5)}, {a -> 8/9, b -> 5/9, c -> 5/9, d -> 0, e -> -sqrt(3/5), f -> sqrt(3/5)}}
```

Figure 21: Screen capture of system solved using Wolfram Mathematica 11.

An alternative method to finding the roots entails first obtaining the coefficients. This can be done using the Legendre polynomials listed at the beginning. The set of polynomial functions P_0, P_1, \dots, P_n defined in the following way is orthogonal on $[a, b]$ with respect to a weight function of one. These polynomials are recursive by nature where $P_0(x) = 1$, $P_1(x) = x - b$ for $x \in a, b$ where,

$$\frac{\int_a^b x[P(x)]^2 dx}{\int_a^b [P_0(x)]^2 dx}$$

and when $k \geq 2$,

$$P_k(x) = (x - B_k)P_{k-1}(x) - C_k P_{k-2}(x)$$

where B_k and C_k can be found using,

$$B_k = \frac{\int_a^b x[P_{k-1}(x)]^2 dx}{\int_a^b [P_{k-1}(x)]^2 dx}$$

$$C_k = \frac{\int_a^b xP_{k-1}(x)P_{k-2}(x) dx}{\int_a^b [P_{k-2}(x)]^2 dx}$$

For example, to find the Legendre polynomial of degree 5 we use the above formulas to find,

$$P_5(x) = (x - B_5)P_{5-1}(x) - C_5 P_{5-2}(x)$$

$$P_5(x) = (x - B_5)\left(X^4 - \frac{6}{7}x^2 + \frac{3}{35}\right) - C_5\left(x^3 - \frac{3x}{5}\right)$$

We have to find B_5 and C_5 using equations 51 and 52.

$$B_k = \frac{\int_{-1}^1 x[P_4(x)]^2 dx}{\int_{-1}^1 [P_4(x)]^2 dx}$$

Integrating this equation we get $B_k = 1$ and we solve for C_5

$$C_5 = \frac{\int_{-1}^1 xP_4(x)P_3(x) dx}{\int_{-1}^1 [P_3(x)]^2 dx}$$

In which we also integrate and substitute back into equation 54 to get,

$$P_5(x) = \frac{1}{8}(63x^5 - 70x^3 + 15x)$$

We can use this polynomial to find the roots by setting the polynomial to zero. This will give the root values seen in the table for n=5.

Roots [x^5 - 6/7 x^3 + 3/35 x - 16/63 x^3 + 48/315 x = 0, x]

$$x = 0 \quad || \quad x = \frac{1}{3} \sqrt{\frac{1}{7} (35 - 2\sqrt{70})} \quad || \quad x = -\frac{1}{3} \sqrt{\frac{1}{7} (35 - 2\sqrt{70})} \quad || \quad x = \frac{1}{3} \sqrt{\frac{1}{7} (35 + 2\sqrt{70})} \quad || \quad x = -\frac{1}{3} \sqrt{\frac{1}{7} (35 + 2\sqrt{70})}$$

Figure 22: Solving for roots of the Legendre polynomial of degree 5.

Using these roots and setting up a system of equations as seen with n=3 we get a system that looks like this:

$$\begin{aligned} C_1 + C_2 + C_3 + C_4 + C_5 &= 2 \\ C_1X_1 + C_2X_2 + C_3X_3 + C_4X_4 + C_5X_5 &= 0 \\ C_1X_1^2 + C_2X_2^2 + C_3X_3^2 + C_4X_4^2 + C_5X_5^2 &= \frac{2}{3} \\ C_1X_1^3 + C_2X_2^3 + C_3X_3^3 + C_4X_4^3 + C_5X_5^3 &= 0 \\ C_1X_1^4 + C_2X_2^4 + C_3X_3^4 + C_4X_4^4 + C_5X_5^4 &= \frac{2}{5} \end{aligned}$$

| i | x_i | w_i |
|-----|---------------------------|---------------------------|
| 1 | -0.9997137267734412336782 | 7.3463449050567173E-4 |
| 2 | -0.9984919506395958184002 | 0.0017093926535181052395 |
| 3 | -0.996295134733125149186 | 0.0026839253715534824194 |
| 4 | -0.993124937037443459652 | 0.0036559612013263751823 |
| 5 | -0.9889843952429917480044 | 0.0046244500634221193511 |
| 6 | -0.983877540706057015496 | 0.0055884280038655151572 |
| 7 | -0.977809358486918288554 | 0.0065469484508453227642 |
| 8 | -0.970785775763706331931 | 0.0074990732554647115788 |
| 9 | -0.962813654255815527294 | 0.0084438714696689714026 |
| 10 | -0.9539007829254917428493 | 0.0093804196536944579514 |
| 11 | -0.944055870136255977963 | 0.0103078025748689695858 |
| 12 | -0.933288535043079545924 | 0.0112251140231859771172 |
| 13 | -0.921609298145333952667 | 0.0121314576629794974077 |
| 14 | -0.9090295709825296904671 | 0.013025947892971542286 |
| 15 | -0.8955616449707269866985 | 0.013907710703718772688 |
| 16 | -0.8812186793850184155733 | 0.014775884527441301769 |
| 17 | -0.8660146884971646234107 | 0.015629621077546002724 |
| 18 | -0.8499645278795912842934 | 0.0164680861761452126431 |
| 19 | -0.8330838798884008235429 | 0.017290460568323582439 |
| 20 | -0.815389238339176254394 | 0.0180959407221281166644 |
| 21 | -0.79689789239031447639 | 0.018883739613374904553 |
| 22 | -0.7776279096494954756276 | 0.0196530874944353058654 |
| 23 | -0.7575981185197071760357 | 0.0204032326462094327668 |
| 24 | -0.7368280898020207055124 | 0.0211334421125276415427 |
| 25 | -0.71533811757305644646 | 0.021843002416247386314 |
| 26 | -0.6931491993558019659487 | 0.0225312202563362727018 |
| 27 | -0.670283015603141015803 | 0.02319742318525412162249 |
| 28 | -0.6467619085141292798326 | 0.0238409602659682059626 |
| 29 | -0.622608860203707771604 | 0.02446120270795705272 |

Figure 23: 26 sets of high accuracy Gaussian Quadrature nodes and weights from the Keisan Online Calculator service provided by Casio ComputerCo., Ltd.

J Runge-Kutta Methods

Runge-Kutta methods are single-steps with multiple stages per step. They depend on Taylor methods of the specific Initial Value Problem (IVP). They are among the most popular Ordinary Differential Equations (ODE) solvers. The family of Runge-Kutta Methods can be defined generally as a collocation method

$$F_i = f(y_n + h \sum_{j=1}^s a_{ij} F_j), i = 1, \dots, s, y_{n+1} = y_n + h \sum_{i=1}^s b_i f(Y_i)$$

Here, s is termed the number of stages of the Runge-Kutta method, the $b_i, i = 1, \dots, s$ are the weights, and the a_{ij} are the internal coefficients. Each Runge-Kutta method generates an approximation of the flow map. Each Y_i in the above equation can be viewed as

$$y_{n+1} = y_n + h \sum_{i=1}^s b_i f(Y_i(y_n, h))$$

The most famous Runge-Kutta method has four stages

$$\begin{aligned} Y_1 &= y_n \\ Y_2 &= y_n + \frac{h}{2} f(Y_1) \\ Y_3 &= y_n + \frac{h}{2} f(Y_2) \\ Y_4 &= y_n + h f(Y_3) \\ y_{n+1} &= y_n + h \left(\frac{1}{6} f(Y_1) + \frac{1}{3} f(Y_2) + \frac{1}{3} f(Y_3) + \frac{1}{6} f(Y_4) \right) \end{aligned}$$

The accuracy of the method in terms of its approximation of a numerical solution over one timestep.

K Gaussian Quadrature Example

To examine the accuracy of this method we can solve this integral whose real answer we already know to be 1.483803256.

$$\int_1^{1.5} \int_0^x (x^2 + \sqrt{y}) dy dx$$

We must convert the interval of the integral on the inside to $[-1,1]$,

$$y = \frac{(x-0)t + x + 0}{2} = \frac{x(t+1)}{2}$$

The formula is used for a change of variables to give,

$$\int_{-1}^1 x^2 + \sqrt{\frac{x(t+1)}{2}} \frac{x}{2} dt$$

wherein t is substituted for roots and we approximate by a sum.

$$\begin{aligned} &\approx \frac{x}{2} \left[x^2 + \sqrt{\frac{x}{2}} (\sqrt{1 + 0.5773502692}) \right] + \frac{x}{2} \left[x^2 + \sqrt{\frac{x}{2}} (t+1) (\sqrt{1 - 0.5773502692}) \right] \\ &\approx x^3 + x^{\frac{3}{2}} (0.6738873387) \end{aligned}$$

We substitute this into the integral on the outside to give,

$$\int_1^{1.5} x^3 + x^{\frac{3}{2}} (0.6738873387) dx$$

and convert the interval to $[-1,1]$.

$$x = \frac{(b-a)t + b + c}{2} = \frac{t}{2} + \frac{5}{4}$$

After another change of variables we have,

$$\int_{-1}^1 \frac{1}{4} \left(\frac{t}{2} + \frac{5}{4} \right)^3 + \left(\frac{t}{2} + \frac{5}{4} \right)^{\frac{3}{2}} (0.6738873387) dt$$

wherein t is substituted for roots and we approximate by a sum.

$$\begin{aligned} &\approx \frac{1}{4} \left(\frac{(0.5773502692)}{2} + \frac{5}{4} \right)^3 + \left(\frac{(0.5773502692)}{2} + \frac{5}{4} \right)^{\frac{3}{2}} (0.6738873387) \\ &+ \frac{1}{4} \left(\frac{(-0.5773502692)}{2} + \frac{5}{4} \right)^3 + \left(\frac{(-0.5773502692)}{2} + \frac{5}{4} \right)^{\frac{3}{2}} (0.6738873387) \end{aligned}$$

This gives an numerical approximation of 1.488874528 which has two decimal places of accuracy compared to our real answer. Nonetheless, the Gaussian Quadrature method is very robust and can be used for many different shapes.